Applying Quantitative Microstructure Control in Advanced Functional Composites

*Nicholas A. Heinz, Teruyuki Ikeda, Yanzhong Pei, and G. Jeffrey Snyder**

Microstructure control in functional materials draws from a historical reserve rich in established theory and experimental observation of metallurgy. Methods such as rapid solidification, eutectoid reaction, and nucleation and growth precipitation have all proven to be effective means to produce microstructure relevant for a wide array of applications. Here, the available parameters to control structure morphology, size, and spacing are discussed using thermoelectric composites as an example. Moreover, exploiting different aspects of a material system's phase diagram enables a controlled introduction of nanostructures. While much of this discussion is pertinent to the rapidly developing field of thermal conductivity control in thermoelectric composites, these techniques can be applied to a variety of other material systems where their use may lead to novel electrical, optical, as well as thermal properties of semiconductors and insulators as it has in the past for the mechanical properties of metals.

1. Introduction

The exploits of the thermoelectric effect have been investigated by scientists for well over a century. Of interest has been the peculiar ability for certain types of materials to convert heat to electricity, or under an applied current, create a temperature gradient as a means of solid state cooling. However, recent interest in the field has been spawned by the ever increasing global energy demand, and exacerbated by the current techniques to supply this demand by means that negatively affect the overall well-being of the planet. Some argue that thermoelectric materials have a low probability of making a significant impact in the realm of alternative sources of energy,[1] while others are more optimistic regarding the possible thermoelectric returns.[2] Both sides agree, however, that in order for this to happen it is necessary for the efficiency of thermoelectric materials to be increased.

Typically when discussing thermoelectric materials, the efficiency is described by the dimensionless Figure of merit (zT). This value controls the individual material's efficiency and can be divided into three main material properties $zT = \frac{\alpha^2}{\rho\kappa}T$, where α is the Seebeck coefficient (also known as thermopower), ρ is the electrical resistivity, and κ is the thermal conductivity which can be broken up into the lattice and electrical portions ($\kappa = \kappa_l + \kappa_e$). Therefore, an ideal thermoelectric material has a large Seebeck coefficient while concurrently being electrically conductive and thermally insulating. This leads to the desire to individually tune these material properties to enhance the Figure of merit. This proves to be quite difficult due to the coupled effects of electrons involved in each property.[3] However, the lattice portion of the thermal conductivity is least affected by the behavior of electrons. Therefore, inhibiting the transport of heat conducted by phonons is a route to increasing the Figure of merit in thermoelectric materials.

The reduction is founded on the idea that if the phonon mean free path, the distance between phonon scattering events, is limited one can achieve appreciable decreases in the thermal conductivity. Early experimental and theoretical indication of the spectral nature of thermal conductivity was conducted at liquid helium temperatures on samples of quartz and KCl.[4,5] The scope of these works was to determine the effects of the crystal bounds on thermal conductivity. Because the phonon mean free path is large enough at such temperatures, the phonons travel ballistically through the material, rarely scattering off each other, rather scattering off the crystal walls. This established a correlation between size and the resulting thermal conductivity and inspired the development of techniques to control thermal conductivity such as alloying[6] and grain size reduction.[7]

Since then, these established techniques have been utilized in a number of material systems,[8–11] and new processing techniques have been developed in an attempt to gain further control of thermal conductivity by controlling dimensionality.[12,13] Renewed interest in the frequency dependence of phonons has inspired the demand for better transport modeling and frequency dependent measurements to adequately characterize such materials.[14,15] This leads to a critical need for a deeper understanding of the role interfaces play at these structure boundaries.[16,17]

Building on these earlier reviews, the focus of this article is to provide a framework to quantitatively characterize

N. A. Heinz, Prof. G. J. Snyder
Materials Science, California Institute of Technology
1200 E. California Blvd. Pasadena, CA, 91125, USA
E-mail: jsnyder@caltech.edu
Prof. T. Ikeda
Materials Science and Engineering
Ibaraki University
4-12-1, Nakanarusawa, Hitachi, 316-8511, Japan
Prof. Y. Pei
School of Materials Science and Engineering
Tongji University
4800 Caoan Rd., Shanghai, 201804, China

DOI: 10.1002/adfm.201302899

microstructure in a way that can be usefully integrated in these advanced thermal transport models. Luckily, microstructure morphology and quantitative characterization has a long history in metallurgy that can be applied to semiconductors. We will discuss the ability to quantitatively control the microstructure and understand the specific parameters relative to microstructural morphology, size, and spacing in composite materials. The proofs of concept for these processes are substantiated through several specific examples on thermoelectric materials. We also describe some of the newer complex characterization tools as well as classic metallurgical analysis techniques pertinent to the quantification of microstructure that will enable the size control needed for the next generation of functional composite semiconductors such as thermoelectrics.

Nicholas Heinz is a PhD candidate in Materials Science at the California Institute of Technology. His research is focused on microstructure control and transport properties of tetradymite structured chalcogenides and other anisotropic compounds. He is interested in pertinent materials design relevant to thermoelectric cooling and low temperature power generation. Prior to Caltech, Nicholas received a B.S. in Mechanical Engineering from the University of Southern California.

Teruyuki Ikeda received his Dr. Eng. degree in Materials Science from Kyoto University in 2000, then worked at Osaka University as a Research Associate. He was then appointed at California Institute of Technology in 2005. He was a PRESTO researcher funded by Japan Science and Technology Agency from 2008 to 2012 staying at Caltech. He is now a Professor of Materials Science and Engineering at Ibaraki University (Japan) since 2013. His current research interests include structural control in various length scales of functional materials.

G. Jeffrey Snyder is a Faculty Associate at the California Institute of Technology (Caltech) in Pasadena California. His interests are focused on the materials physics and chemistry for thermoelectric engineering, such as band engineering, design of complex Zintl compounds and use of nanostructured composites. His interdisciplinary approach stems from studies of Solid State Chemistry at Cornell University and the Max Planck Institute for solid state research, Applied Physics at Stanford University and thermoelectric materials and device engineering at NASA/Jet Propulsion Laboratory.

2. Structure Types

A practical starting point for understanding microstructural evolution is in identifying the type of structure formed in one of the many available processing routes. There are many structure types where direct observation is often enough to identify, while others are difficult to differentiate and requires additional information. Often the origins of these difficult to differentiate structures are resolved by understanding the driving force behind the phase separation. This is typically done by determining the phase diagram of the material in question through experiments and calculations. The following descriptions are not intended to be a comprehensive list of structure types, rather the intent is to introduce the types of structures often encountered in the course of tuning thermal conductivity.

2.1. Grain Size Reduction

One avenue avidly pursued to reduce the lattice thermal conductivity is to minimize the grain size via mechanical alloying/milling (**Figure 1**a) and rapid consolidation techniques. In these works, powders are created by ball milling ingots of pre-melted materials (mechanical milling) or the pure elements (mechanical alloying). In both cases, the grain size is reduced to tens of nanometers and is maintained at that size by using rapid consolidation. The composite aspect of these materials usually lies in slight compositional differences, which manifest themselves in the form of component rich ingrain nanoparticles.[8] There is also evidence to suggest that small impurities at the grain boundaries exist in these types of materials[18] that could inhibit grain growth.

The first system in which thermal conductivity dependence on grain size was studied was in alloys of Si–Ge.[7] It was found that a grain size of 5 μm or less resulted in a 28% decrease in thermal conductivity compared to the single crystal value. Since then, work has been done in Bi_2Te_3/Sb_2Te_3, PbTe, Skutterudites and further enhancements in Si–Ge have been achieved in this fashion.[8]

2.2. Grain Boundary Phase

Controlling grain boundary phases is a fairly new and relatively unexplored route to creating functional thermoelectric composites. The current state of the art uses coated powders and hot pressing consolidation to achieve these structures (Figure 1b).[16] There have been several thermoelectric systems that have been explored in this fashion such as PbSnSe coatings

© 2013 WILEY-VCH Verlag GmbH & Co. KGaA, Weinheim

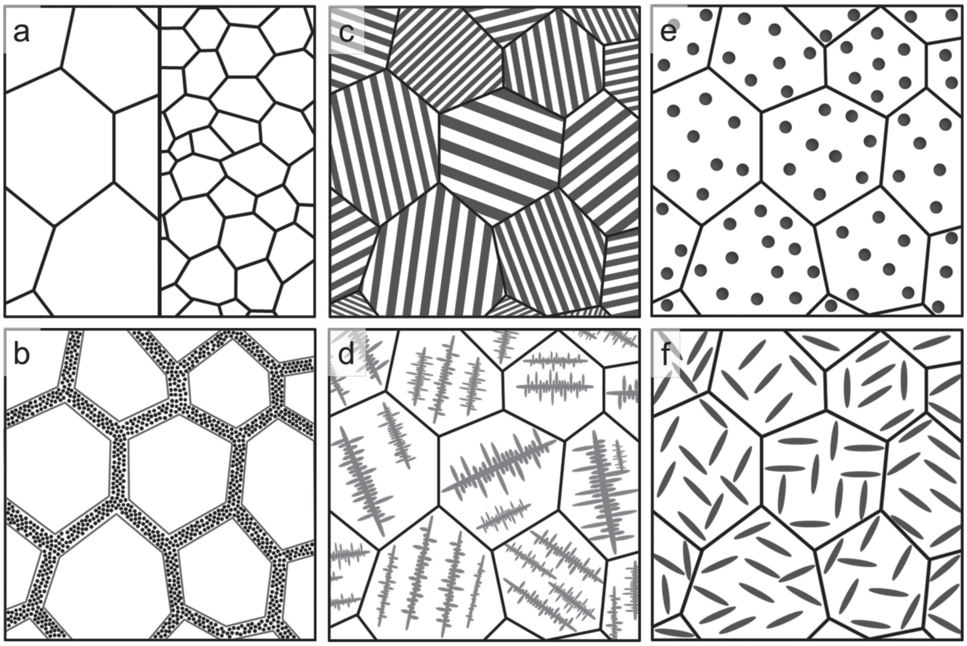

Figure 1. Examples of different types of deliberate microstructure in thermoelectric applications. a) Grain size reduction, b) grain boundary phases, c) lamellar structures, d) dendrite formation, and e,f) precipitation based microstructure are all promising routes to reducing thermal conductivity.

on PbSnTe and also $CoSb_3$ coatings on $LaCoFe_3Sb_{12}$.[19,20] Initial studies on alkali-metal coated $(Bi,Sb)_2Te_3$ materials have shown improvements in zT due to a reduction in κ_l as well.[21] However, more work is necessary to understand the structure controlling and carrier scattering mechanisms in these materials because there is evidence of thermal conductivity reduction even in systems with an incomplete grain boundary phase present.[22]

2.3. Lamellar and Dendritic Structures

Lamellae are finely spaced (nm–μm) structures that alternate in composition as shown in Figure 1c. They resemble superlattice structures often generated through thin film techniques, with the added advantage of being self-assembled. Lamellar structures can be either completely aligned in a given domain (as in Figure 1c) or can have more of a disordered pattern. The most prevalent material studied with such a structure is pearlite steel,[23] but this type of structure has formed in the $PbTe–Sb_2Te_3$ system of materials as well.[24–27] This type of microstructure can be generated in the bulk by solidification and eutectic reactions or through solid state techniques such as eutectoid reactions.

Dendrite structures can also be generated by solidification methods and have a tree-like branched form (Figure 1d). In geology, dendritic formation can occur in the large scale crystal habit, as is the case for native copper. However, in materials design dendrites are more typically thought of as a result of an internal phase separation. Analogous to lamellae, dendritic microstructure has been found in the $PbTe–Sb_2Te_3$ system, however unlike the lamellae, dendrites are typically formed by solidification from the liquid.[25,27]

2.4. Precipitates

Nucleation and growth techniques are often used to grow precipitates within grains with varying morphology (Figure 1e,f). Typically the decreasing solubility with decreasing temperature of eutectic, or eutectic-like, phase diagrams is the procedure for growing structures of this type. Systems with high solute solubility (>3 at%) are often desired as this can correlate to a higher number density of precipitates. A high second phase solubility also indicates that the volume fraction will be large enough to have a significant impact on κ_l. Ideally, simple eutectic, or eutectic-like phase diagrams present approachable ways to exploit the decreasing solubility with decreasing temperature along the solvus line to precipitate out the desired second phase. This often allows for fine structure on account of the temperature control in the two phase region, and also the slow diffusion in the solid state. There has been extensive work done with this technique in age hardening of metals,[28] but recently this technique has proven beneficial in the PbTe system in conjunction with Ag_2Te, Sb_2Te_3, and also $PbBi_2Te_4$.[29–33]

3. Morphology Control

For each previously mentioned structure type there are different ways to vary the resulting microstructure's morphology. From a seemingly simple binary phase diagram, one can achieve several different structure types by varying the chemical composition, solidification rate, or processing route. Typically, areas around invariant points associated with solidification reactions, such as eutectic or peritectic points, act as morphology transition indicators for different microstructure types.

© 2013 WILEY-VCH Verlag GmbH & Co. KGaA, Weinheim

3.1. Solidification Morphology

The point on a phase diagram in which a single phase liquid directly solidifies into solid phases, forgoing any solid–liquid equilibrium region, is referred to as the eutectic point. In discussing binary, or in many thermoelectric cases pseudo-binary, eutectic solidification the microstructural morphology is most easily understood using the ideas of Hunt and Jackson.[34] Early atomistic treatments of solid–liquid interface growth by Jackson considered the free energy change during the atom exchange for an exposed crystal face in contact with its liquid during melting or freezing.[35,36] It was determined that the material's entropy of fusion, ΔS_f, also known as the entropy of melting, can be used to predict morphology type. The entropy of fusion,

$$\Delta S_f = \frac{\Delta H_f}{T_m} \tag{1}$$

where ΔH_f and T_m are the enthalpy of fusion and the melting point, is the change in entropy upon melting of a pure substance. Under this formalism,[36] the entropy increases as the configurational possibilities increase as melting occurs, thus the value is often positive.

The entropy of fusion is made dimensionless when divided by the universal gas constant ($\chi = \frac{\Delta S_f}{R}$) and when the free energy change associated with the atom exchange during growth is minimized, there are two distinct mechanisms based on χ. For values of $\chi < 2$ the free energy is minimized resulting in a rough crystal interface indicative of no preferential crystal ordering, and for $\chi > 2$ the minimization dictates a smooth interface, representative of a preferred crystal orientation during growth.[35]

It should be specified that the following criteria pertain to solidification at or near the eutectic point, which will be referred to as eutectic solidification. Eutectic compounds can be placed into three discernible categories based on χ.[34] The first is where the entropies of fusion of the two substances are similarly low ($\chi < 2$), the next is where they are completely dissimilar ($\chi < 2$ in one, $\chi > 2$ the other), and the third is where both are similarly high ($\chi > 2$).

In the case of the constituent compounds having low ΔS_f values, the morphology is most often lamellar or rod-like. Examples of this type of behavior exist in such systems as Pb–Sn, Pb–Cd, or Sn–Cd[34] where each compound has a similar enthalpy of fusion and melting point (**Table 1**).

There is a more varied morphology, however, when one phase has a lower ΔS_f than the other. The structures in this scenario often have a complex and or irregular shape. Classic cases of such morphologies can be seen in the Pb–Bi or Sn–Bi systems[34] as the low melting point and large enthalpy of fusion give Bi a significantly larger χ than either Sn or Pb (Table 1).

In the case of similarly large ΔS_f values, both phases grow with smooth solid–liquid interfaces under a normal nucleation process, which often results in large flat crystal faces. On account of semi-metals or semi-conducting materials often having high entropies of fusion, this type of microstructure is observed in the solidification of such materials.

The atomistic view in the previous discussion works well for simple systems such as metals, however when more complex compounds are considered the total molar content can be misleading with regard to ΔS_f. To extend the predictive guidelines of the entropy of fusion for more complex material systems, it is necessary to convert the units from a per mole basis to one that is per moles of atoms. Also known as the gram-atom (g-atom), this is done simply by dividing the enthalpy of fusion by the number of moles of constituent atoms in one mole of the compound. This conversion takes into account the fact that enthalpy and entropy are extensive properties, and it puts the comparison of simple metals and more complex systems on an even keel by effectively normalizing them by the total number of moles of atoms in one mole of the compound. Therefore, as seen in Table 1 the values of ΔS_f for the elemental metals and semi-metals is the same, however for the binary and ternary compounds is decreased by the number of moles of atoms.

Table 1. Enthalpy and entropy of fusion per g-atom, and χ values for simple metals and more complex compounds pertinent to the discussion of solidification morphology.

Compound	T_m [K]	ΔH_f [kJ g-atom^{-1}]	ΔS_f [kJ g-atom^{-1} K]	χ	Refs.
Pb	600.6	4.77	7.95	0.96	[38]
Sn	505.1	7.15	14.15	1.70	[38]
Cd	594.2	6.21	10.45	1.26	[38]
Bi	544.6	11.11	20.39	2.45	[38]
Si	1687.2	50.21	29.76	3.58	[38]
Ge	1211.4	36.94	30.49	3.67	[38]
Sb_2Te_3	891.2	19.8	22.2	2.67	[39]
PbTe	1197.2	20.7	17.3	2.08	[40]
TiO_2	2143	22.32	10.41	1.25	[41]
$CaTiO_3$	2233	21.3	9.6	1.15	[42]
$BaTiO_3$	1898	15.9	8.4	1.01	[43]

In some cases however this conversion is not sufficient to explain the resulting morphology. In the case of the eutectic solidification of TiO_2-$SrTiO_3$ the resulting structures upon solidification have been proven to be faceted, resembling that of split ring resonators.[37] However, as can be seen in Table 1 after the g-atom conversion, the values for TiO_2 and two other titanates comparable to $SrTiO_3$ all have values of χ below the transition value for faceted structures. However, upon melting these highly ionic materials the resulting liquid is not completely disordered. Therefore, there is an additional consideration to make for molecular liquids, as there is a significant ordering required upon freezing.

While ΔS_f is a good indicator for whether the growth interface will be diffuse or smooth, resulting in lamellar/rod-like or faceted structures, it does not always predict the resulting solidification morphology. When the solidification occurs at a composition that is far from the eutectic composition, the effects of undercooling play an important role in the solidification morphology. Currently, the impact of undercooling on eutectic solidification has been explored on a preliminary basis, and it has been established that there exists a critical undercooling where the morphology differs from the type predicted by

© 2013 WILEY-VCH Verlag GmbH & Co. KGaA, Weinheim

ΔS_f.[44] There is continued work in understanding the mechanism in which this change occurs.[45]

However, many applications either allow or require that solidification take place far from the eutectic composition, and the mechanism for freezing of this variety is known as single phase solidification. That is, there is one primary solidifying phase, unlike eutectic solidification in which there are at least two. In the solidification of a eutectic system far from the eutectic composition, the solid phase rejects solute at the solidification front, thereby increasing the solute content in the liquid and decreasing the liquid temperature in the vicinity of the solid–liquid interface. Therefore, the temperature of the liquid at the interface will be lower than the liquidus temperature of the bulk liquid and this effect is known as constitutional undercooling.

This concentration gradient based undercooling can lead to variations in the resulting morphology in single phase solidification. The source of the variation stems from the solid–liquid interface stability. Tiller and Chalmers determined that for a binary single phase solidifying system, in the absence of convection, there is a critical condition in which constitutional undercooling occurs[46]

$$\frac{\nabla T}{v} \leq \frac{mC_0}{D}\left(\frac{1-k}{k}\right) \tag{2}$$

where ∇T is the temperature gradient in the liquid at the interface, v is the solidification velocity, m is the slope of the liquidus, C_0 is the equilibrium concentration, D is the diffusion coefficient, and k is the distribution coefficient. For values of $\frac{\nabla T}{v}$ that do not satisfy this condition, it is predicted that the solidification will result in no microstructure formation. However, for values of $\frac{\nabla T}{v}$ that satisfy this condition there will be some form of microstructure generation. Moreover, if the value of $\frac{\nabla T}{v}$ is near the critical condition the likely morphology will be that of a lamellar or rod like structure, often referred to as a cellular structure. When the departure from this critical value is large, the morphology is typically dendritic. It should be noted that ΔS_f is still an important parameter in single phase solidification. In that, if faceted structures are predicted, and the value of $\frac{\nabla T}{v}$ is sufficiently small, the resulting microstructure will still be atomically smooth, but can produce faceted dendrites[47] or spiraled hopper crystals.[48]

Taking this into account, the solidification morphology of single phase solidification has been explored in the more complex PbTe–Sb_2Te_3 system.[25,27] After the g-atom conversion this material system behaves as one would with dissimilar values of χ. As can be seen in **Figure 2**, when rich in the lower ΔS_f -PbTe phase, the resulting microstructure is dendritic, while when rich in the higher entropy Sb_2Te_3 phase the microstructure is of a layered and faceted variety. This happens in lieu of the fact that in both materials χ is greater than the transition value. However, because the value for PbTe is very near this transition point it is not unreasonable to find a non-faceted microstructure.

The degree of structure alignment can be controlled in solidification based microstructure formation as well. The formation of eutectic microstructure occurs at the solid–liquid interface, and directional solidification results in an aligned microstructure. In this process the entirety of the material is melted and one end is brought into a zone of decreased temperature initiating solidification. This proceeds until the solid–liquid interface reaches the other end of the sample, solidifying completely. Successful lamellar alignment has been accomplished in the Ag–Pb–Te and Ag–Sb–Pb–Te ternary systems utilizing this method.[49,50] All of the same morphological control parameters are employed (ΔS_f and $\frac{\nabla T}{v}$) in this type of experiment, however because the solidification is directional, the interface control is substantial, allowing one to tailor the alignment of the resulting microstructure. Often, the scenario of low ΔS_f values involving lamellar or rod-like morphology have the most significant alignment due to the simplicity of growth compared to that of irregular or faceted structures.

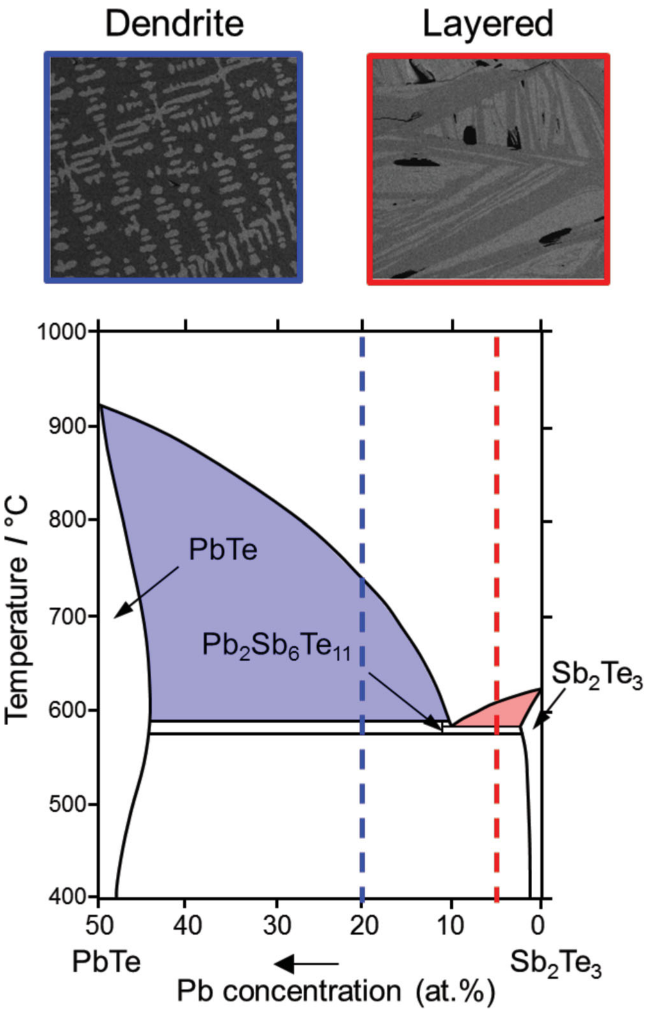

Figure 2. Even in the same material system it is possible to generate different microstructure based on the details outlined in Equations 1,2. In the case of the pseudo-binary PbTe-Sb_2Te_3 system, to the PbTe side of the eutectic solidification experiments yield a dendritic microstructure, while to the Sb_2Te_3 portion experiment yield a layered faceted microstructure.[25] Adapted with permission.[27] Copyright 2010, The Minerals, Metals & Materials Society.

© 2013 WILEY-VCH Verlag GmbH & Co. KGaA, Weinheim

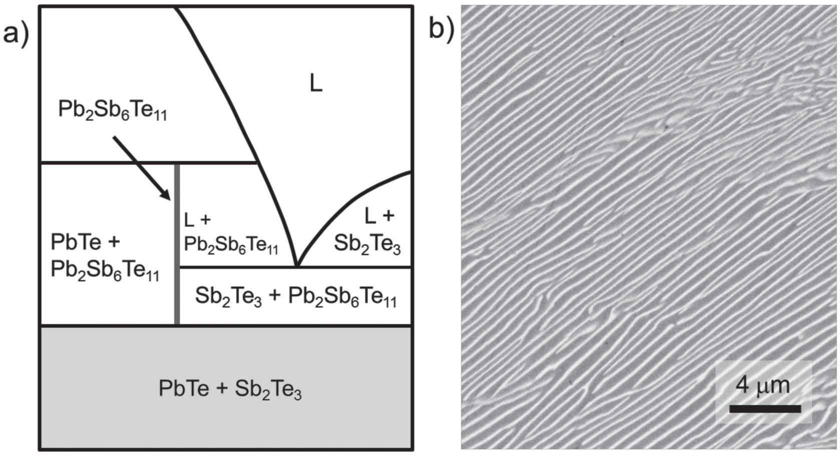

Figure 3. a) A magnified section of the PbTe-Sb_2Te_3 phase diagram near the $Pb_2Sb_6Te_{11}$ eutectoid compound[27] and b) an electron micrograph of the resulting directional cooling experiments for the eutectoid reaction of $Pb_2Sb_6Te_{11}$ to PbTe-Sb_2Te_3. The resulting microstructure is aligned in a similar fashion to the directional solidification experiments that were the basis of the morphological control.[34] Adapted with permission.[27] Copyright 2010, The Minerals, Metals & Materials Society.

3.2. Eutectoid Reaction Morphology

While eutectic solidification involves a single liquid transforming into two (or more) solids upon cooling, a eutectoid reaction is similar and produces similar microstructure. The difference being that the latter reaction pathway involves a single solid dissociating into distinct solid phases. There is a similar type of microstructure formed by a reaction known as spinodal decomposition.[51] It is often however difficult to differentiate between lamellar eutectic/eutectoid structures and those formed by spinodal decomposition. The difference lies within the formation pathways, the former involving growth via nucleation[52] and the latter occurring uniformly throughout.[51] Distinguishing between the two reactions directly would involve the impractical in-situ observation of the microstructural evolution. More practically, understanding the phase diagram would reveal the nature of the microstructure's origin. An example of a thermoelectric spinodal is that of the PbTe–GeTe system,[53] and while this type of microstructure has been shown to be effective in tuning thermal conductivity it does not fall under the scope of this work.

There is a rich history of directional solidification experiments examining the alignment and morphology of the resulting microstructure,[34] but this is not the case with regard to eutectoid reactions.[54–57] However, it is possible to extend the results of the directional eutectic solidification literature to better understand eutectoid reactions with the added exception of understanding the role of interfacial strain energy. Because the material remains in the solid state throughout a eutectoid reaction, the interfacial interactions are non-negligible[58] complicating eutectoid reactions due to transformation strain at the solid-solid interfaces.

The results of eutectoid directional cooling experiments can be seen in **Figure 3** where the metastable $Pb_2Sb_6Te_{11}$ phase reacts to form lamellae of PbTe and Sb_2Te_3. A more isotropic morphology is possible when the material is annealed at a temperature below the eutectoid point, which can be seen in Figure 8. Therefore, the anisotropy of the resulting structures can be controlled via the reaction interface through directional cooling (isotropic structures) or bulk isothermal annealing (anisotropic structures) depending on which type is desired.

3.3. Nucleation and Growth Precipitation Morphology

The generation of microstructure based on nucleation and growth of precipitates is described best by the labeled eutectic phase diagram of **Figure 4**. In accordance to this type of phase diagram, a typical synthesis route to precipitate a secondary β phase in a matrix of α would be to first melt the constituent elements, then homogenize the material in the solid solution region and finally precipitate the desired microstructure.

The initial morphology of precipitates formed during nucleation and growth is best understood based on the dependence of free energy. Nucleation occurs when the overall change in free energy is lowered causing ΔG to be a negative value. To first order, ΔG is represented by

$$\Delta G = -V\Delta G_V + A\gamma \tag{3}$$

where V is the nuclei volume, ΔG_V is the volumetric free energy, A is the nuclei surface area, and γ is the surface free energy. For the stable nuclei initially formed, the morphology

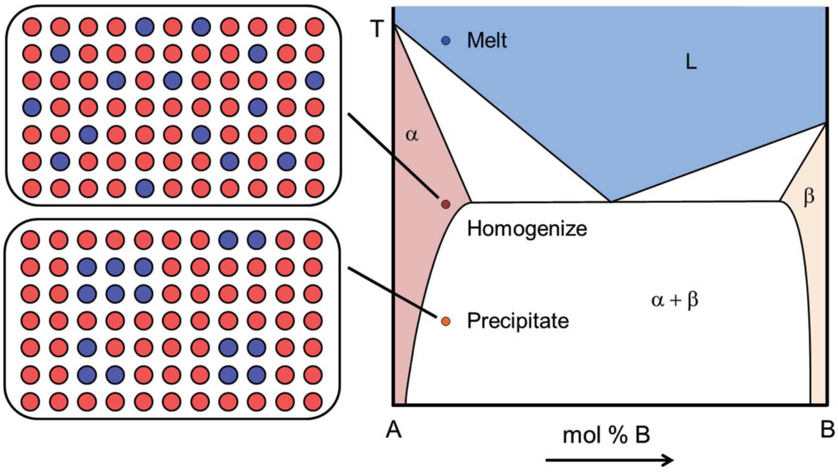

Figure 4. A schematic of the processing route undertaken in nucleation and growth based microstructure formation. The material is initially melted, then homogenized, and finally the isothermal annealing temperature is decreased such that it exploits the decreasing solubility with temperature to form a second phase.

© 2013 WILEY-VCH Verlag GmbH & Co. KGaA, Weinheim

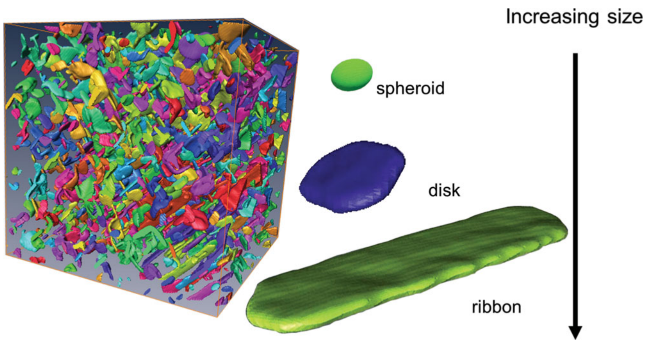

Figure 5. A three dimensional reconstructed SEM image of a PbTe-Sb_2Te_3 section and the resulting size dependent morphologies. As the size of the precipitate increases the morphology changes from a spheroid to a disk and finally a ribbon like morphology[60]

will be spheroidal to balance the dominance of the surface free energy to that of the volumetric free energy (Equation 3 and **Figure 5**). As the precipitates grow, however, the optimization of the volumetric and interfacial free energies can lead to a myriad of morphologies as the dominant shape of the resulting precipitates is not necessarily an equilibrium shape. Often, the resulting stable structures are the ones that nucleate the fastest.[59] This occurs due to the strong dependence of γ on the nucleation rate, which does not necessitate an equilibrium shape as it could very well be a less stable structure that dominates the growth process.

There are also interfacial elastic energies, based on the elastic constants, that can play a role in governing the morphology of precipitates in this regime.[58] As has been seen in the PbTe–Sb_2Te_3 system, a weak interfacial compatibility condition led to precipitates forming a ribbon like shape as opposed to the disk or lenticular shape previously expected (Figure 5).[60]

However, other simple guidelines for precipitation based morphology lie in the comparison of crystal structures and lattice constants of the materials in question. For example, in the Bi–Sb system both elements share the same crystal structure and have very similar lattice parameters, so based on the Hume Rothery rules it is not unexpected for them to form a complete solid solution and ultimately little, if any, microstructure.[61] However, Bi and As also share the same crystal structure yet the lattice mismatch is large enough that there is very little solubility[62] indicating the possibilities of significant nucleation based microstructure formation.

However, many examples of nucleation and growth based microstructure in thermoelectric materials is one of differing crystal structures. The differing morphological results are often dictated by which material is the host phase, and which is the secondary phase. In both the PbTe–Sb_2Te_3 and $AgSbTe_2$–Sb_2Te_3 systems the host phase is a rock-salt structured crystal with an embedded tetradymite secondary phase,[63,64] each with the classic FCC-HCP $\{111\} \parallel \{0001\}$orientation relationship. The primary difference however, is in the dislocation spacing along the interface in each system. Due to the large mismatch (6.7 %) in the PbTe–Sb_2Te_3 system[63] there are a significant number of interfacial dislocations along the interface (arrows, **Figure 6**). However, the lattice mismatch in $AgSbTe_2$–Sb_2Te_3 is an order of magnitude smaller (0.8 %)[64] and has an appreciably lower interfacial dislocation content, so much so that it is difficult to directly image.

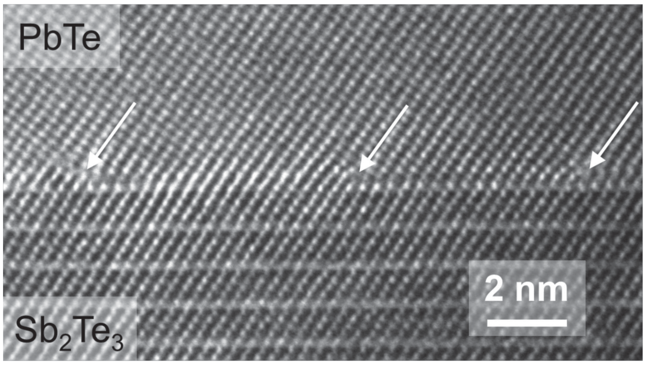

Figure 6. A high resolution transmission electron microscope (HRTEM) image of interfacial dislocations at the boundary of Sb_2Te_3 (bottom) in PbTe (top). The arrows indicate the location of the dislocation cores at the interface.

Some systems' combination of crystal structure and lattice mismatch even allow for coherent precipitation to occur, as all previous cases were reported to be semi-coherent. In the case of PbTe–Ag_2Te, it has been reported that the cubic-monoclinic arrangement of $\{001\} \parallel \{201\}$ and a low lattice mismatch of 1.8% permits complete coherency in some precipitates.[65] The morphological evolution in this system is slightly complicated as the nucleation and growth temperatures involve cubic phases for both PbTe and Ag_2Te, while upon cooling the Ag_2Te phase transforms into the monoclinic phase.

In all of the previously mentioned cases, the host or matrix phase has been a cubic structure and since there are often several similar crystallographic orientations, four in the $\{111\} \parallel \{0001\}$ case (top row, Figure 15) and three in the $\{001\} \parallel \{201\}$ case, there is often a distribution of structure orientations. However, the Bi_2Te_3–In_2Te_3 system, while having a $\{111\} \parallel \{0001\}$ orientation, is limited to the precipitation in the basal planes as the matrix phase is the HCP crystal. Therefore, the resulting microstructure is aligned with all precipitates oriented in the same fashion in any individual grain (bottom row, Figure 15).

3.4. Nonequilibrium Processing Morphology

Nonequilibrium processing provides additional dimensions of control in material systems in which equilibrium based processing routes do not. The resulting morphology is created by initially forcing a system into a metastable state, and then rapidly bringing it back into equilibrium (detailed in Figure 16). However, akin to the discussion of free energy balancing in nucleation and growth for nuclei formation, the initial shape to balance out the free energy is typically spheroidal due to the small structure size.

This is most likely due to the inherent large chemical driving force in compounds with large heats of solution, increasing the nucleation rate and ultimately the number density. Under the assumption of spherical nuclei and the fact that the equilibrium volume fraction will be fixed by the phase diagram, the structure size is expected to be small, possibly approaching the critical radius for stable nuclei, r^*, according to

$$f_v = \frac{4}{3}\pi r^3 N_v \quad (4)$$

where f_v is the volume fraction, r is the nuclei radius, and N_v is the number density. Therefore, for a fixed value of f_v and an increase in N_v due to the increased nucleation, the nuclei radius will decrease. If the increase in N_v is large enough, it is possible for the actual structure radius to be near the value of the critical radius, r^*. Thus, as discussed in the previous section, the balancing of the volumetric and surface free energies results in a spheroidal morphology (Figure 17).

4. Control of Length Scale and Implications

It is important to describe quantitatively what the definition of fine microstructure is for thermoelectric materials. The early works in Si–Ge alloys claimed that significant reductions can be achieved at a mean structure size of 2 μm.[7,66,67] While this may be true in Si–Ge alloys, the spectral nature of thermal conductivity dictates that structure size and scattering is material dependent, arising from the varied phonon dispersions in different material systems. Therefore, it is reasonable to expect an array of structure sizes and spacings can benevolently affect κ_l for thermoelectric applications. In PbTe for example, calculations were conducted with the conclusion that 80% of the heat carrying phonons had a mean free path that spanned nearly two orders of magnitude (50–1000 nm).[68] Moreover, other authors calculated that if the phonon mean free path was limited to 100 nm in PbTe, there would be a 20% reduction in the total thermal conductivity.[15] It was further asserted that to achieve a thermal conductivity reduction of 40% in PbTe would involve decreasing the phonon mean free path an order of magnitude further to 10 nm. These works elucidate the idea that it is possible to achieve a significant thermal conductivity reduction through structure sizes and spacings larger than recently predicted,[11,14] but smaller than originally thought.[66,67,69]

4.1. Solidification

Solidification of materials at or around critical points, such as eutectic or peritectic reactions, has been known to produce a spectrum of different microstructure types. Even though the resulting microstructural differences often dictate morphology specific parameters to fully quantify the structures, one universal parameter that controls length scale during solidification is the cooling rate, R_{LS}. It is in understanding the cooling rate that can lead to information about the onset and completion of solidification and also quantifiable predictions to size scales of the potential structures.

In order to quantify the cooling rate, R_{LS}, during solidification it is necessary to identify the initiation and termination points of solidification. This information is garnered from experimental T versus t cooling curves. In the simplest case, the material should experience thermal arrest during solidification. Specifically at the points of initiation and completion, the cooling curve will exhibit local extrema in $\frac{dR_{LS}}{dt}$. If we assume a simple binary eutectic phase diagram, it would be expected that the initiation and completion stages would occur at the liquidus (initiation) and eutectic (completion) temperatures. From the T versus t curves, the onset of solidification will be a local minimum due to the significant drop in cooling rate as the material traverses from the pure liquid to the solid–liquid region, as it will no longer be compensated by the latent heat of fusion, and the cooling rate will increase once again. Once the onset and completion temperature and time have been well defined, it is a simple matter of calculating $R_{LS} = \frac{\Delta T_{LS}}{\Delta t_{LS}}$.

Once the cooling rate is established, it is possible to be quantitative about controlling the resulting structural features. Cooling rate effects on structure size has been extremely important for improving the yield strength in metals and has been studied extensively.[70] In the case of the PbTe–Sb_2Te_3 thermoelectric system, Ikeda employed the inter lamellar spacing, or layer spacing, λ, for the layered faceted structures and secondary dendritic arm spacing, d_s, as characteristics to compare microstructural sizes.[25] Inter lamellar spacing is the spacing between the central points of the areas of compositional discontinuity. More simply put, it is the spacing between the center points of two adjacent structures in the material. This is calculated for many structures, in many domains across the material. Obviously this trait only applies to materials in which layered structures are the primary type. Secondary dendritic arm spacing is the spacing between the secondary arms that form on dendritic structures. This can be imagined as the primary dendrite arm as a saw blade, and the secondary arms as the teeth on the blade.

Cooling rate is often empirically described for dendritic systems related to d_s by[71]

$$d_s \propto \frac{1}{R_{LS}^n} \quad (5)$$

where n is an empirical constant and R_{LS} is the liquid–solid cooling rate. The value of $n = 0.32$ in PbTe–Sb_2Te_3 is similar to those reported in the literature, as typical values of n range from 0.25 for most Al alloys up to 0.48 for Sn–Pb alloys.[25] In looking at Equation 5 it is obvious that for a system of primarily dendritic microstructure formation, the larger the solidification rate the finer the microstructure.

The determining factors controlling the inter lamellar spacing however are not as straightforward. The layer spacing, λ, for a simple eutectic reaction during nucleation is described by[72]

$$\lambda^2 v \propto \text{const.} \quad (6)$$

where v is the solidification velocity. According to Equation 6, λ is expected to decrease for an increased solidification velocity. It is a reasonable assumption that this is directly related to the cooling rate, therefore a larger cooling rate will decrease the layer spacing. However, there is an inherent drawback to using solidification techniques with thermoelectric materials due to their low thermal conductivities as it leads to low solidification velocities. For example, to achieve structure sizes on the order of what is typically desired (≈100 nm) in the PbTe–Sb_2Te_3 system, this would require a cooling rate upwards of 10^5 K s^{-1},[25] which

© 2013 WILEY-VCH Verlag GmbH & Co. KGaA, Weinheim

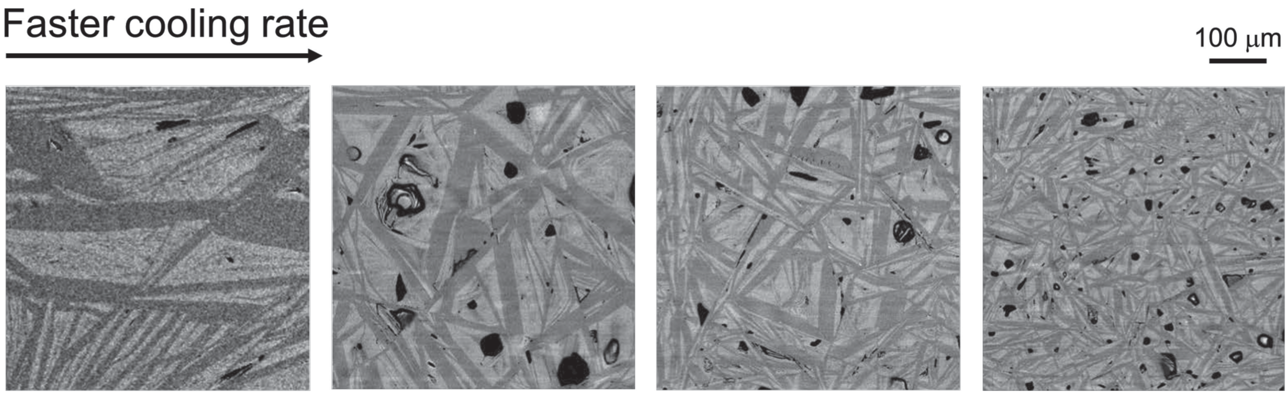

Figure 7. The trend of smaller structure size with increased cooling rate is seen in the solidification experiments of Ikeda involving PbTe-Sb_2Te_3[25,27]

can be difficult to achieve when the internal heat transfer of the solidifying material is low.

Still, results of measurements in the PbTe–Sb_2Te_3 system involving the structure size dependence on solidification rate support the idea that a faster cooling rate results in finer microstructure (**Figure 7**). Even though the PbTe–Sb_2Te_3 system's inherent low thermal conductivity requires a very large cooling rate for thermoelectric applications, there are techniques that could potentially achieve this. Splat cooling is a candidate that involves rapidly solidifying a thin layer of liquid on a cooled surface.[73] A version of splat cooling called melt spinning[74] has been widely used in the amorphization of materials, most notably metallic glasses.[75] Melt spinning has been used in thermoelectric materials, however the focus tends to be in making nanocrystalline material.[76,78] There has been a recent trend in attempting to correlate the effect of cooling rate on the resulting transport properties,[79,80] however quantitative microstructure control is often not considered.

4.2. Eutectoid Reaction

Controlling microstructure formation via eutectoid reaction works on the idea that if one starts with a solid phase that becomes metastable below some critical temperature, it is possible to generate fine microstructure through the decomposition of this metastable phase into two new, energetically favorable phases ($\gamma \rightarrow \alpha + \beta$). Similar synthesis routes can be used in peritectoid reactions, with the difference being that the metastable phase separates upon an increase in temperature beyond the critical point. However, here the focus will remain on eutectoid reaction based microstructure formation. The parameters for controlling the microstructure size and spacing are the time for the reaction to take place and the temperature at which the event occurs. Early metallurgical works in Cu–Al alloys[54] and Co, Cu, and Ni alloys[57] laid the groundwork in establishing that a large undercooling results in a fine layer spacing in eutectoid systems. With regard to thermoelectric materials, we visit the PbTe–Sb_2Te_3 system and find that the starting metastable compound $Pb_2Sb_6Te_{11}$ will react to form lamellae of PbTe and Sb_2Te_3 (**Figure 8**).

The complexity of the inter lamellar spacing during nucleation makes for difficult modeling, however there have been several investigations to model the coarsening of eutectic and eutectoid microstructure. Graham and Kraft modeled $\lambda(t)$ of the Al–$CuAl_2$ eutectic system based on fault migration[81] which lead to a linear time dependence ($\lambda(t) \sim t$) of the lamellar spacing. Cline used a similar approach to model coarsening, however also included fault annihilation and derived a $t^{1/2}$ dependence.[82] However, the data for the PbTe–Sb_2Te_3 system did not present a linear time dependence with respect to lamellar spacing. In fact, as can be seen in **Figure 9**, there was a decelerated coarsening with time, which is better represented by the power law developed by Cline ($t^{1/2}$) but even this still did not fit well with the data.[26]

In order to better understand the coarsening method in the PbTe–Sb_2Te_3 system it would be beneficial to obtain more kinetic data and develop more thorough models. A route to enhance existing models could be to incorporate a Kolmogorov-Johnson-Mehl-Avrami (KJMA)[83–87] like equation to the methods of either Graham and Kraft[81] or Cline.[82] The KJMA equation, which takes the form

$$f = 1 - \exp(-kt^n) \tag{7}$$

and represents the percentage of volume fraction transformed in nucleation and growth based microstructure, could establish a more realistic deceleration in lamellar spacing.

The temperature dependence of lamellar spacing was very well described by Zener[72] in his studies of the kinetics of austenite decomposition. He developed the idea that the layer spacing at the onset of coarsening is related to the undercooling by

$$\lambda = \frac{4\gamma T_{\mathrm{E}} V_{\mathrm{m}}}{\Delta H \Delta T} \tag{8}$$

where γ is the surface energy, T_{E} is the eutectoid temperature, V_{m} is the molar volume, ΔH is the enthalpy difference between the eutectoid and supercooled material at the onset of nucleation, and ΔT is the undercooling. This expression implies that the further below the eutectoid temperature the reaction takes place, the smaller the layer spacing. This idea is well supported by the λ data of PbTe–Sb_2Te_3 (Figure 9) as the lamellar spacing decreases as the undercooling increases. The benefits of resulting spacing due to the large undercooling can be seen in the lattice thermal conductivity data (**Figure 10**) as well, where there is a large decrease in κ for large ΔT. The

© 2013 WILEY-VCH Verlag GmbH & Co. KGaA, Weinheim

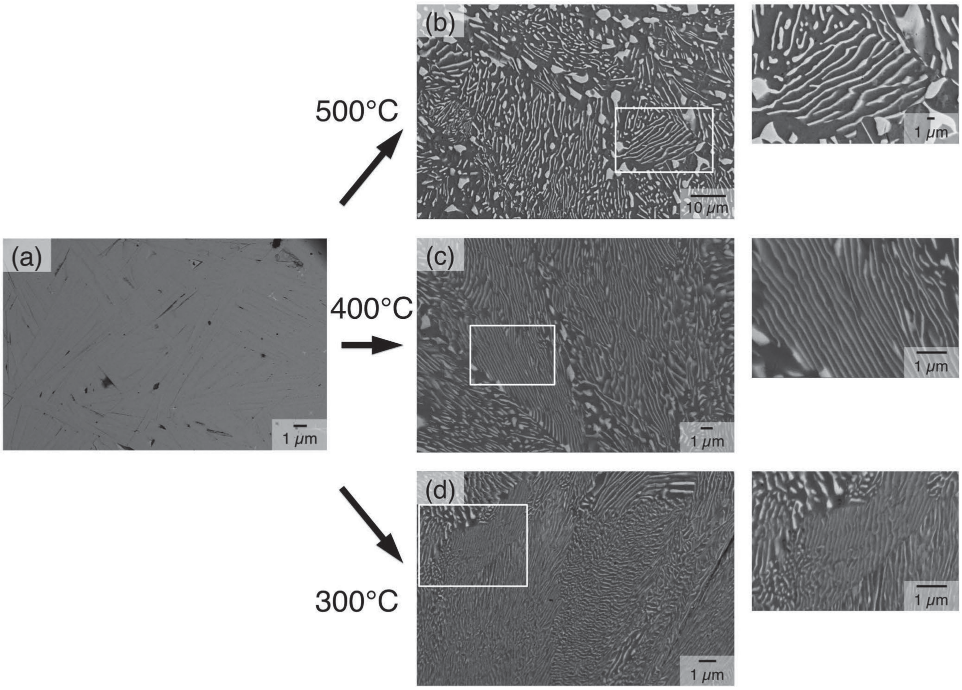

Figure 8. The trend of decreasing layer spacing with larger undercooling is observed in the case of the eutectoid reaction of a) $Pb_2Sb_6Te_{11}$ to $PbTe–Sb_2Te_3$. The three examples annealed for equivalent time at b) 500 °C, c) 400 °C, and d) 300 °C validate the assertions of Equation 8.

temperature dependence of this spacing is limited, however, as it is unlikely that for extremely large undercoolings the reaction kinetics will allow significant microstructure formation. The beginning of such a limitation can be seen in Figure 9, as the dependence of λ on the reaction temperature decreases for the samples below 500 °C.

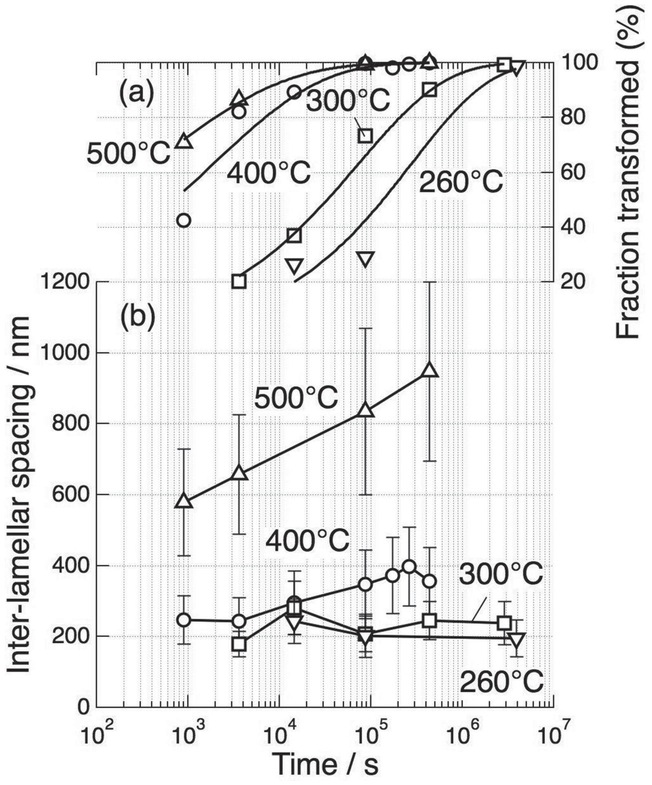

Figure 9. The a) fraction transformed and b) inter-lamellar spacing, λ, vs time for several samples of $PbTe–Sb_2Te_3$.[26] The discrepancy among the samples involved could potentially be remedied with the generation of a KJMA type equation (see text).

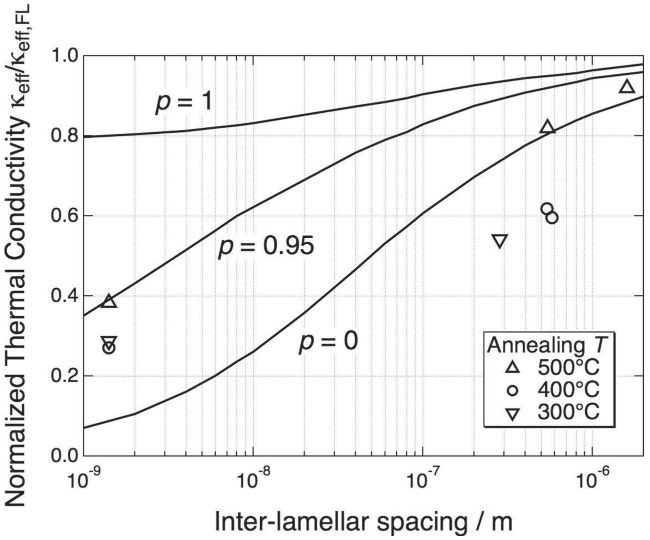

Figure 10. The dependence of thermal conductivity on the layer spacing in the $PbTe–Sb_2Te_3$ system shows a dramatic improvement when the layer spacing is minimized.[88] The values of p indicate the level of specularity with values near zero being diffuse. Adapted with permission.[88] Copyright 2010, American Institute of Physics.

© 2013 WILEY-VCH Verlag GmbH & Co. KGaA, Weinheim

A secondary parameter to tune would be the surface, or interface energy, γ. Due to the inherent difficulty in directly tuning the surface energy, it is more a consideration that can be taken to promote smaller lamellar spacings that are beneficial for thermoelectrics. For example, if the two constituent materials involved in the reaction are known to have low energy incoherent interfaces, this could be an important deciding factor that can help reduce the inter lamellar spacing.

There is also the added benefit of eutectoid reactions over eutectic reactions for thermoelectric applications because of the kinetic nature of solid state reactions. Diffusion in the liquid state is considerably faster than in the solid state, so when a eutectoid reaction takes place, the diffusion is markedly slower. The end result of such diffusion is that the resulting microstructure often has a higher number density for a similar volume.

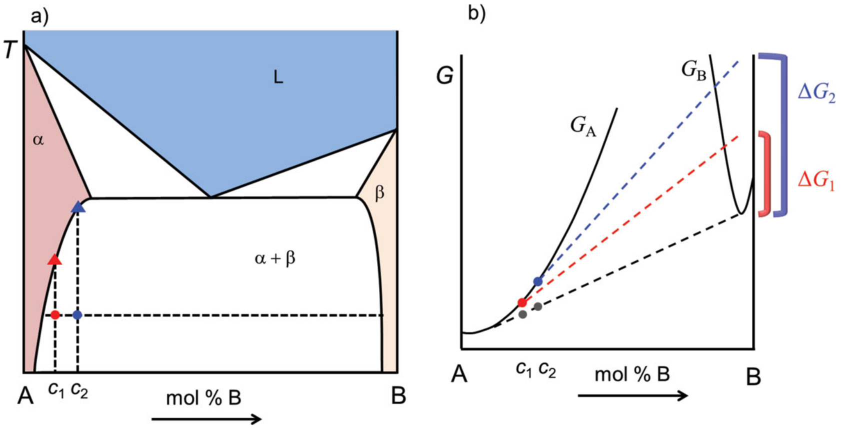

Figure 11. A schematic of a) a typical binary eutectic phase diagram portraying the effects of altering the composition for a given temperature and b) the resulting free energy curves and chemical driving force difference resulting from a change in supersaturation. A larger supersaturation will lead to a larger chemical driving force, and ultimately stronger nucleation, leading to finer microstructure formation. The red and blue triangles in (a) assist in the description of the effects seen in Figure 13.

It should be noted that measured layer spacing for in-grain lamellae is strongly dependent on the orientation relative to the viewing plane. Lamellae that lie perpendicular to the viewing plane will appear to have a smaller layer spacing than those that are not. Therefore, when measuring layer spacing, it is necessary to account for this discrepancy and calculate the true lamellar spacing.[89]

4.3. Nucleation and Growth Precipitation

Because the synthesis procedure for nucleation and growth based precipitation as described in Figure 4 is also a solid state reaction, it has the same microstructural advantages as that of eutectoid microstructure. However, the nucleation and growth of precipitate based microstructure is dependent on three parameters. The temperature at which the phase segregation takes place, the composition of the material based on the phase diagram, and the duration of the event all control the resulting size and spacing during the transformation. This type of microstructure formation is often used with great success in the strengthening of Al[90] and Fe[91] alloys and is often referred to as age or precipitate hardening.[92] There is an overlap in control parameters between eutectoid and nucleation and growth based reactions, however, in the latter case the composition is not as limited by critical points on the phase diagram, therefore allowing more variability in the volume fractions of constituent phases.

There is, however, a compositional limitation set by the phase diagram for nucleation processes. If a eutectic phase diagram is considered, this limitation is dictated by the maximum solubility of the secondary phase in the host material. As can be seen in Figure 4, a typical synthesis route to precipitate a secondary β phase in a matrix of α would be to first melt the constituent elements, then homogenize the material and finally precipitate the desired microstructure. Therefore, it is imperative to have a strict understanding of the solvus line (the line separating the α or β phases from the $\alpha + \beta$ region) to quantitatively control the resulting microstructure. Unidirectional solidification experiments, such as the Bridgmann method, can be used to determine the maximum solubility,[31,33,93] and isothermal annealing experiments can be conducted to map out the pertinent portions of the solvus line.

Once there has been some determination of the solvus line, it is necessary to understand the effects of undercooling (ΔT) and supersaturation (Δc). In this case, the undercooling is defined as the difference in temperature from the solvus line and the temperature of the material when $T < T_{\text{solvus}}$. The supersaturation on the other hand corresponds to the amount of excess solute in the material when $c > c_{\text{solvus}}$.

Figure 11 a is a schematic of a binary eutectic phase diagram, and the corresponding free energy curves associated with the isotherm indicated by the horizontal dashed line (Figure 11b). It is assumed that the two compositions considered have a similar undercooling with the main difference being the supersaturation levels; with one having a higher solute content than the other ($c_2 > c_1$).

As can be seen in Figure 11b, the lowest free energy curve for compositions c_1 and c_2 is the common tangent, indicating that the lowest energy configuration dictates a phase separation. Moreover, the chemical driving force, which is related to the tangent of G_α (at c_1 or c_2) to the composition near the tangent point of G_β, increases as the composition is increased from c_1 to c_2. Therefore, the larger chemical driving force for c_2 (ΔG_2) indicates there will be a stronger drive for nucleation than c_1 (ΔG_1).

This supersaturation trend can be seen in the nucleation and growth work done within the PbTe–Ag_2Te system (**Figure 12**).[30] The Ag_2Te content was increased in four increments over the same isotherm, and resulted in an increased number density due to the increased nucleation driven by the larger supersaturation. Because of this, there was a large reduction in the thermal conductivity reduction as seen in Figure 12 and was the basis for improving both n- and p-type PbTe.

The variable composition cooling experiments in the PbTe–Sb_2Te_3 system (**Figure 13**) had slightly contradictory results,

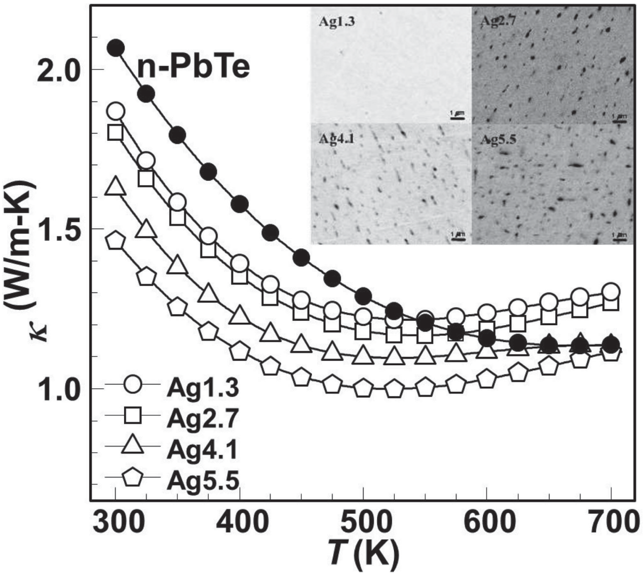

Figure 12. The increased supersaturation for a given temperature lead to stronger nucleation, finer microstructure and eventually a lower κ in the case of PbTe-Ag$_2$Te. Adapted with permission.[30] Copyright 2012, Wiley-VCH.

however.[32] Two similarly structured samples of different composition were analyzed and the lower solute concentration sample resulted in a larger number density, which would imply a larger chemical driving force. However, the synthesis routine consisted of slow cooling (10 K h^{-1}) as opposed to isothermal annealing, and the larger solute containing sample's solvus temperature was higher, schematically depicted with triangles in Figure 11a, which lead to a longer duration in the two-phase region and significant coarsening. This is an example of how the undercooling and supersaturation can change simultaneously, which makes decoupling their effects difficult.

Despite this difficulty however, it is possible to describe the effects undercooling in the context of the critical free energy and radii of nucleation. From a thermodynamic standpoint, in order for nucleation to occur there must be an overall lowering of the free energy due to the volume of the second phase formed. This is opposed by the increase in free energy due to the surface energy between the matrix and secondary phase. In nucleation during solidification, these are the important terms that dominate the phase formation, however in solid state nucleation there is a misfit strain relation to consider because the newly formed phase often does not fit perfectly into the allotted volume on account of differing lattice parameters, crystal structures, and often both.

Taking into account this misfit strain, the total free energy change (ΔG) is altered from Equation 3 to

$$\Delta G = \frac{4}{3}\pi r^3\left(-\Delta G_{\mathrm{V}} + \Delta G_{\mathrm{S}}\right) + 4\pi r^2 \gamma \tag{9}$$

where γ is the surface free energy, and ΔG_{V} and ΔG_{S} are the volumetric and strain free energy terms. If a spherical nucleus is assumed, then the critical radius, r^*, and critical free energy for nucleation, ΔG^*, are

$$r^* = \frac{2\gamma}{\left(\Delta G_{\mathrm{V}} - \Delta G_{\mathrm{S}}\right)} \tag{10}$$

and

$$\Delta G^* = \frac{16\pi\gamma^3}{3\left(\Delta G_{\mathrm{V}} - \Delta G_{\mathrm{S}}\right)^2} \tag{11}$$

where ΔG_{V} is proportional to ΔT, which is the undercooling. The temperature dependence of these critical values can be seen schematically in **Figure 14** as the undercooling is inversely proportional to both. The expected trend of finer microstructure with larger undercooling is observed in several thermoelectric systems, as seen in **Figure 15**, including but not limited to PbTe–Sb$_2$Te$_3$ and Bi$_2$Te$_3$–In$_2$Te$_3$.[32,94] In these cases the precipitate size and spacing decreased drastically as the undercooling increased for various annealing temperatures.

Based on the thermodynamic equations describing undercooling, it would be expected that arbitrarily increasing the undercooling would correspond to a proportional increase in nucleation. For long annealing times this may be true, however, there are kinetic limitations to consider. For example, increasing the undercooling such that it approaches absolute zero would not likely result in significant microstructure formation in most materials due to the lack of diffusion at such temperatures. In fact, due to the balancing of thermodynamics and kinetics, the fastest nucleation rate is often at an intermediate undercooling.[95]

In practice it is commonly difficult to separate the effects of supersaturation and undercooling because of the slope of the solvus line. As can be seen in Figures 11, 14, as one changes either the annealing temperature or the composition, it simultaneously affects both the undercooling and supersaturation. Therefore, from a materials architecture

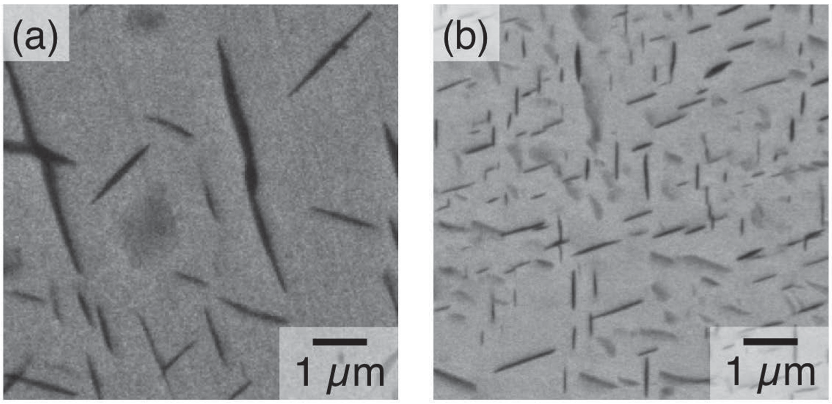

Figure 13. Resulting scanning electron microscope (SEM) images of two samples of PbTe–Sb$_2$Te$_3$ where a) had a starting composition of 5.5 at% Sb and b) 4 at%.[32] However, these samples were prepared by slow cooling as opposed to isothermal annealing, and the a) 5.5 at% sample was in the two phase region longer than the b) 4 at% sample (as depicted by the difference between the circles and triangles for c_1 and c_2 in Figure 11a). The resulting microstructure suffered in (a) due to significant coarsening despite the higher supersaturation.

© 2013 WILEY-VCH Verlag GmbH & Co. KGaA, Weinheim

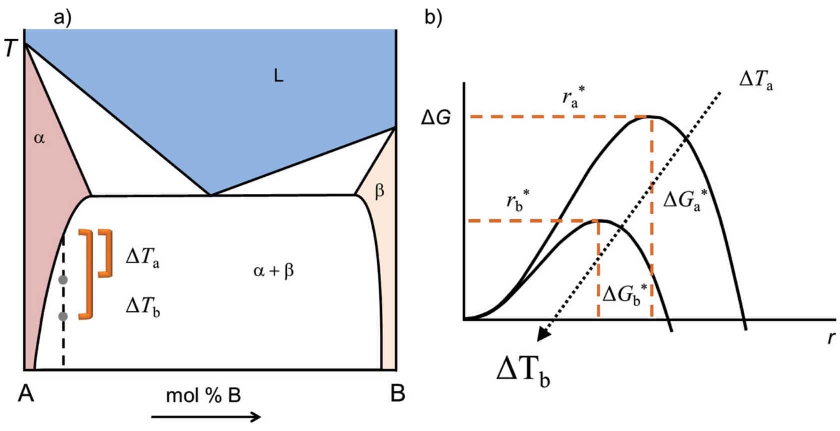

Figure 14. A schematic of a) a typical binary eutectic phase diagram portraying the effects of altering the temperature for a given composition and b) the resulting free energy vs critical radius curves for the two examples. For a larger undercooling, there is a decreased critical nucleus size for continued nucleation, therefore an increase in nucleation events leading to finer microstructure.

standpoint, it is necessary to establish the degree of sensitivity of each parameter by conducting individual studies of both undercooling and supersaturation to attempt to determine which has the greatest influence regarding microstructure optimization.

Fortunately there is a simple and effective determining length scale to judge how rapid nucleation is, and also when nucleation is complete. This information lies in the characteristic diffusion length l

$$l \propto \sqrt{Dt} \tag{12}$$

where D is the temperature dependent diffusion coefficient of the solute, and t is the time in which the diffusion at this temperature takes place.

According to the soft impingement effect,[59] when the distance between precipitates is less than or equal to l it is expected for nucleation to have reached its conclusion. This should be treated as an order of magnitude approximation, but is an important feature because of its simplicity. For example, if the diffusion coefficient of a secondary phase diffusing in a host matrix material is known, it can be estimated how long it would be necessary to anneal a sample to reach complete nucleation for a desired structure spacing. For materials with very low diffusion coefficients this can save an experimentalist a large amount of time in determining the best candidate for microstructure formation.

There is room for improvement regarding the tuning of the interfacial area per unit volume, an important parameter in thermal conductivity control. For thermoelectric applications it is desired to have a large interfacial area per unit volume as it has been shown that this results in a large reduction in κ.[15,96] However, in nucleation and growth, altering the supersaturation and undercooling only significantly alters the number density. Assuming geometrical similarity for the same morphological microstructure (maintaining the same aspect ratio, volume fraction, and average diameter to inter-plate distance),[32] the three dimensional limitation to interfacial area per unit volume is governed by

$$A_V = C N_v^{1/3} \tag{13}$$

where A_V is the interfacial area per unit volume, C is a constant and N_V is the number density of precipitates. In order to improve the ratio of interfacial area to volume by a factor of two, it would involve an eight fold increase in the number density, a demand that often times far outreaches the possibilities in a nucleation and growth based scheme. Therefore, unless the interfacial area to volume is naturally in the optimal regime to allow for significant thermal conductivity control, it is difficult to significantly alter A_V via supersaturation and undercooling alone.

However, material selection in and of itself can be considered a control parameter. The heat of solution is directly proportional to the chemical driving force (ΔG in Figure 11b),[97]

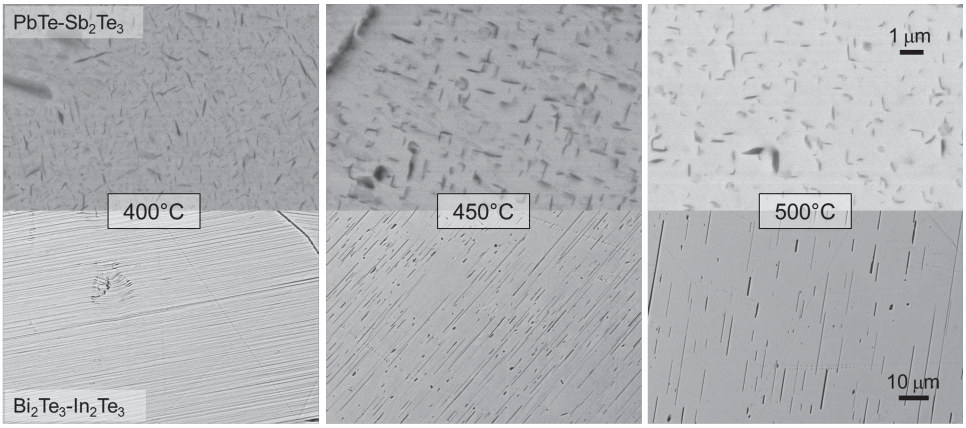

Figure 15. Resulting electron micrographs of the $PbTe–Sb_2Te_3$[32] (top row) and $Bi_2Te_3–In_2Te_3$[94] (bottom row) systems showcasing the effects of increased undercooling for a given composition. In both cases, the microstructure becomes finer for a larger undercooling.

© 2013 WILEY-VCH Verlag GmbH & Co. KGaA, Weinheim

Table 2. The number density, N_v, and heats of solution, ΔH_s, for Ag_2Te and Sb_2Te_3 in PbTe.

Precipitate	T [C]	t [h]	N_v [μm^{-3}]	ΔH_s [kJ g-atom^{-1}]	Refs.
Ag_2Te	500	72	55 ± 30	14.0 ± 3.5	[30,93]
Sb_2Te_3	450	38	15 ± 3	4.4 ± 0.2	[33,93]

whereby a larger heat of solution leads to a larger chemical driving force, and stronger nucleation. Therefore, a precipitating candidate with a large heat of solution can be chosen as this acts to increase the intrinsic value of N_V. This is evident when comparing the number density data of PbTe–Ag_2Te and PbTe–Sb_2Te_3. For comparable annealing temperatures and annealing times the number density of the Ag_2Te structures outnumbers that of Sb_2Te_3 as seen in **Table 2**. This is due to the fact that ΔH_s is much higher for Ag_2Te than Sb_2Te_3 in PbTe.

4.4. Nonequilibrium Processing

In the previous section it was discussed that a large heat of solution leads to a large chemical driving force for nucleation, which in turn results in a large precipitate number density (Table 2). However, materials with large heats of solution tend to have little solubility and typically form line compounds. Therefore, eutectoid and the typical nucleation and growth reactions are insufficient methods to produce a second phase necessary for thermoelectric applications in these types of materials.

Fortunately, steps have been made via metastable nonequilibrium processing, such as rapid solidification (RS), mechanical alloying (MA), and mechanical milling (MM) to improve such solubility limits. Turnbull described the methods as routes to "energize and quench" the metastable states.[98] The techniques involve imparting enough energy to the material ("energize") to take it far from equilibrium and then attempt to retain this configuration ("quench"). In an RS process the far from equilibrium energized state is the (disordered) liquid state, or more specifically, it is the amorphous solid state that forms immediately after quenching, and rapid cooling attempts to maintain the far from equilibrium state. In MA/MM, the energized state is the localized highly disordered state where the milling media comes into contact with the material and there is very little lattice relaxation after this event (if any) due to the low processing temperature.

As can be seen in **Figure 16**a, when the material at composition c_1 is at temperature T_2, the liquid state has the lowest free energy, thus this high entropy state is the most stable. However, if the cooling rate is rapid enough (Figure 16b), immediately after quenching the energized free energy curve (G_{en}), which could be a metastable crystal structure or amorphous state, is reached and even though G_α is not the lowest energy configuration, the system can rest in this metastable state because it has a lower free energy than the previously occupied energized state. This scenario occurs if T_1 is low enough to prevent phase decomposition, which would require long range diffusion. The relaxation from G_{en} to G_α is possible because it can occur via short range diffusion, therefore, there can be short range lattice relaxation and the material can be maintained on the G_α curve, as seen by the middle point in Figure 16b, thus increasing the solubility from c_e to c_1.

The free energy curves look very similar for MA/MM compared to RS processes as can be seen in Figure 16 c. During an MA/MM process, milling media (often stainless steel spheres) constantly fractures and welds material. As depicted in Figure 16c, a material at composition c_1 that undergoes a milling event is locally brought up to the energized state, and after enough time (≈20–100 h)[99–101] all of the material is brought up to this energized state. Just like in RS, this state can be either a metastable crystal structure or an amorphous state, however unlike rapid solidification, MA/MM processes have an easier time maintaining this state because the reaction kinetics are significantly slower on account of the low processing temperature.

Also different than RS processing is that the increased affected surface area in MA/MM events results in the ability to take a material further from equilibrium than is usually possible by rapid solidification. This is beneficial as the further from equilibrium state leads to a larger solubility extension for

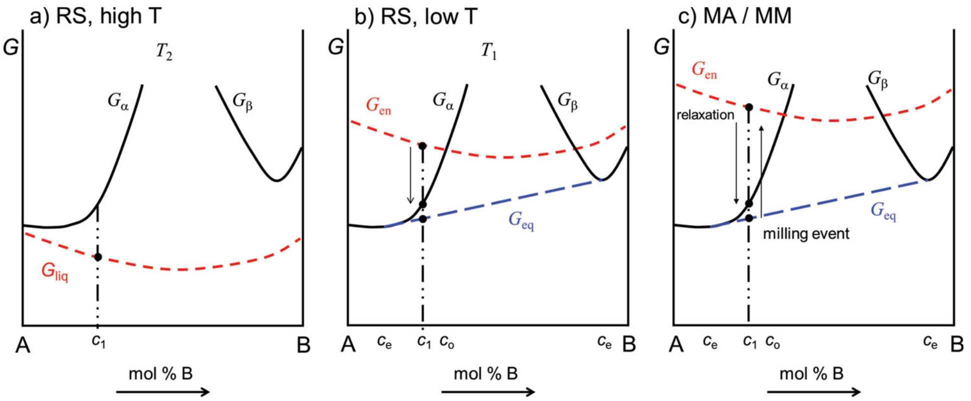

Figure 16. A schematic displaying two different nonequilibrium processing routes. In a) rapid solidification (RS), the system is initially in the liquid state, but immediately upon quenching at a rapid enough rate the system can be stabilized in a nonequilibrium position on the free energy curve (b). However, in (c) mechanical alloying or mechanical milling (MA/MM) the system is gradually brought up to this energized state, and is often an easier route on account of the decreased processing temperature than in RS.

© 2013 WILEY-VCH Verlag GmbH & Co. KGaA, Weinheim

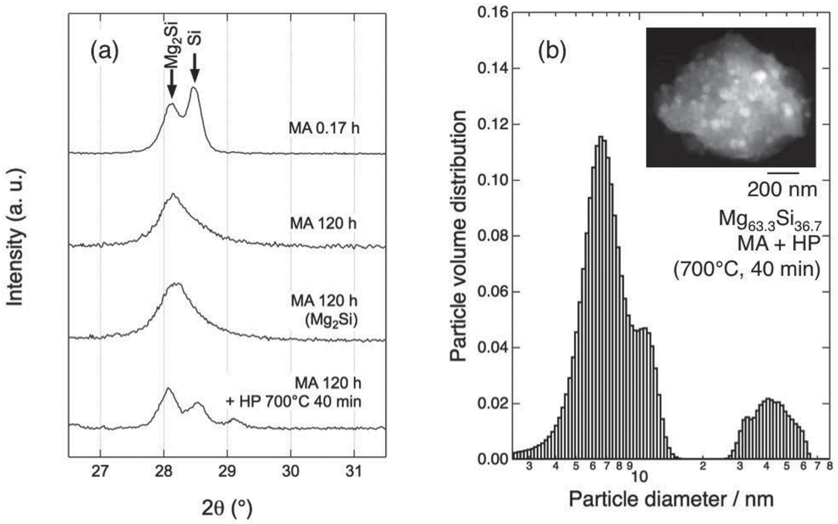

Figure 17. The results of a) X-ray diffraction (XRD) and b) small angle X-ray scattering (SAXS) measurements for $Mg_{63.3}Si_{36.7}$ prepared by nonequilibrium processing. Inset in (b) is a transmission electron microscope (TEM) image of the resulting Si microstructure. The XRD patterns indicate that the additional Si either dissolves in the Mg_2Si or becomes sufficiently small to broaden the two peaks into one. The resulting TEM and SAXS measurements quantitatively showcase the extremely fine scale in which the Si particles form during the consolidation step. Adapted with permission.[102] Copyright 2012, Wiley-VCH.

systems with a larger heat of solution. Finally, since thermal conductivity severely limits the solidification rate, it can be difficult to achieve the cooling rates necessary to increase the solubility in an RS process as thermoelectric materials tend to have very low thermal conductivities.

Additionally, nonequilibrium processing decreases the microstructural restrictions set by the equilibrium phase diagram. By superseding the equilibrium solubility limit it allows for a wider array of nanostructuring elements to be chosen that may have not been possible by equilibrium methods. This is especially true for materials that have large energy requirements to reach a nonequilibrium state, such as in line compounds.

An example of a thermoelectric material that is a line compound with a large heat of solution is Mg_2Si. It was shown that upon Si excess ($Mg_{63.3}Si_{36.7}$) and significant milling times (120 h) it was possible to eliminate the pure Si peaks from the X-ray diffraction spectra, whereby upon consolidation via hot pressing, the Si and Mg_2Si peaks would revert back to the normal spectrum resulting in fine microstructure (**Figure 17**).[102] It is not known whether this was due to an amorphization of the material, or if the size of the Si particles became sufficiently small to broaden the peaks in the X-ray spectra, however transmission electron microscopy (TEM) and small angle X-ray scattering (SAXS) measurements verified nanoparticle formation, and established the resulting bimodal size distribution peaking at values of 7 nm and 40 nm, consistent with the TEM results. It was shown that through this technique the lattice thermal conductivity (κ_l) could be significantly reduced relative to pure Mg_2Si, however further work is needed to control the electron mobility and oxidization from the extended milling to use this material in a thermoelectric application.

5. Microstructure Characterization

Microstructure quantification relies heavily on characterization techniques in order to make suitable conclusions about the resulting structures. It is beneficial to know what techniques are available and also which are appropriate to use at a given time. In characterizing lamellar structures by scanning electron microscopy for example, the observed spacing as obtained from micrographs is not the true value. In fact, unless the lamellae are completely parallel to one another and perpendicular to the observation plane the spacing will be skewed as shown in **Figure 18**a. Fortunately, the experimentally determined lamellar spacing distribution can be straightforwardly fit to[89]

$$F = \frac{\int_{\lambda_1}^{\lambda_2} N_\lambda \, d\lambda}{\int_0^\infty N_\lambda \, d\lambda} \tag{14}$$

where F is the fraction of lamellar spacings for a given interval ($\Delta\lambda$) and N_λ is the number of lamellar spacings, with

$$N_\lambda = \frac{1}{\lambda^3}\left(\int_0^\lambda e^{-\frac{\left(\lambda_0-\lambda_{0,\mathrm{avg}}\right)^2}{2\sigma^2}} \frac{\lambda_0^2}{\sqrt{\lambda^2-\lambda_0^2}} d\lambda_0\right) \tag{15}$$

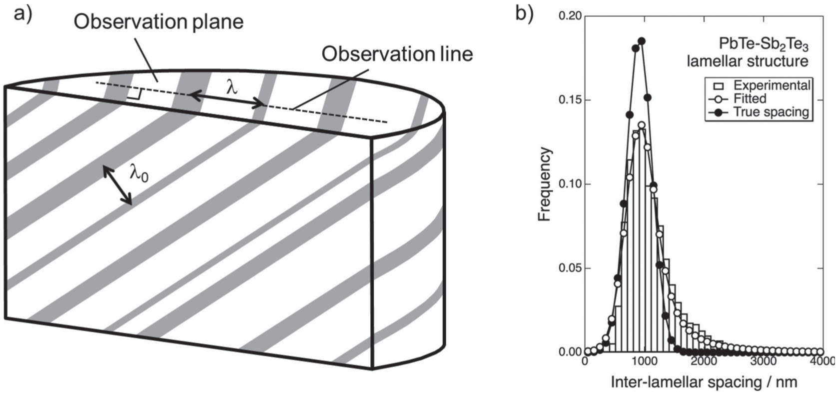

Figure 18. a) Schematic showing the difference in observed lamellar spacing and true lamellar spacing for a sample in which the observation plane is not perpendicular to the lamellae. b) A plot of the lamellar spacing distribution experimentally determined from SEM images, fit by Equations 14,15, and calculated using a Gaussian distribution based on the parameters $\lambda_{0,\mathrm{avg}}$ and σ. Figure adapted with permission.[89] Copyright 2008, Materials Research Society.

Table 3. Major microstructural morphologies and their quantification techniques.

Morphology	Process Reaction	Quantity	Inter-relation	Interface density
Grain Size	Powder metallurgy Solidification	Grain diameter, d	—	$3d^{-1}$[a]
Grain boundary phase	Powder metallurgy Solidification + Precipitation	Grain diameter, d Thickness, t Volume fraction, f_v	$f_v = 3dt^{-1}$	$6d^{-1}$[a,b,c]
Dendrite	Solidification	Secondary dendrite arm spacing, d_s	—	—
Lamellae	Eutectic Eutectoid	Interlamellar spacing, λ Lamellar width, t_1, t_2 Volume fraction, f_1, f_2	$\lambda = t_1 + t_2$ $f_1 = t_1\lambda^{-1}$ $f_2 = t_1\lambda^{-1}$ $f_1 + f_2 = 1$	$2\lambda^{-1}$[d]
Modulated Structure	Precipitation, Spinodal decomposition	Wavelength, L Volume fraction, f_v	—	—
Rod precipitates	Eutectic Eutectoid Monotectic Monotectoid Precipitation	Number per volume, N_v Rod diameter, d Rod length, l Volume fraction, f_v	$f_v = N_v l \pi \left(\frac{d}{2}\right)^2$ $f_v = N_p \pi \left(\frac{d}{2}\right)^2$ N_p	$4f_v d^{-1}$[e]
Plate precipitates	Precipitation	Number per volume, N_v Area per plate, A_p Thickness, t Volume fraction, f_v	$f_v = N_v A_p t$	$2f_v t^{-1}$[e,f]
Spherical precipitates	Eutectic Eutectoid Monotectic Monotectoid Precipitation	Number per volume, N_v Diameter, d Volume fraction, f_v	$f_v = \left(\frac{4}{3}\right) N_v \pi \left(\frac{d}{2}\right)^3$	$6f_v d^{-1}$

[a] d is equivalent sphere diameter. Other model shapes can be found in the literature;[106] [b] For $t \ll d$; [c] Phase boundary density, which is two times the grain boundary area per volume, is shown for A_v; [d] The interlamellar spacing should be the "true" interlamellar spacing;[89] [e] Only the large surface is taken into account; [f] Phase boundary density, which is two times the plate area per volume is shown for A_p.

where λ, $\lambda_{0,avg}$, and σ are the apparent lamellar spacing, average true lamellar spacing, and the standard deviation of the average true lamellar spacing. Once the values of $\lambda_{0,avg}$ and σ are determined it is possible to calculate the true lamellar spacing distribution, as can be seen in Figure 18b for the PbTe-Sb_2Te_3 system. This method is valid when the true lamellar spacing distribution is Gaussian and for regions of the SEM images in which the microstructure is lamellar. This method breaks down for areas in which the lamellae have coarsened and or the transformation mechanism results in non-lamellar microstructure. In such cases there is a technique developed by Cahn and Fullman[103] that necessitates a larger sample size, however with sufficient data converges to the true spacing distribution. The issues in determining true vs apparent spacings exist for other morphology types as well, and there are other established methods in determining those values.[32]

Transmission electron microscopy has also been used to incorporate pertinent quantities of observed defects, such as dislocation density, boundary length, and precipitate size/spacing[104] into established thermal models[105] to better understand the correlations of microstructure and lattice thermal conductivity. Although, a word of caution about transmission electron microscopy preparation is necessary in the discussion of microstructure observation. In PbTe based specimens, it was determined that artificial nanoscale "features" can be created during the ion milling step of materials preparation. It was discovered that unless the sample was cooled to a range of 140–160 K artificial features of a similar size and morphology were created.[65] Therefore it is important to be aware the potential artifacts that can be created, intentional or otherwise.

Quantities which can characterize the size scales pertinent to these structuring techniques are summarized in **Table 3**. A direct way of measurement is to analyze the two dimensional micrographs and convert the results to three dimensional quantities using stereological relations.[106] Number density, N_v (per volume), for example, can be evaluated from the two dimensional N_A (number density per area) using the stereological relation $N_v = N_A d^{-1}$, where d is the average feature size. This value varies depending on the feature morphology as d for spherical particles is the diameter[106] and it is the radius for circular plates.[32]

In order to obtain statistically sound information for a given sample, it is necessary to analyze a large number of micrographs. In SEM observations, caution should be exercised if the size scale is in the nanometer range since the samples may become transparent to the incident beam. Otherwise, such quantities as number density, N_v, volume fraction, f_v,

© 2013 WILEY-VCH Verlag GmbH & Co. KGaA, Weinheim

or feature size, d, of structure phases can be overestimated. Therefore, it is necessary to establish methods to corroborate the independent techniques. Volume fractions of constituent phases (f_i) can be obtained by the Rietveld analysis of powder X-ray diffraction (XRD) spectra and volume fraction can be calculated in systems that have established phase diagrams via the lever rule. To obtain information regarding size scales such as feature size, d, thickness, t, or spacing, l, powder XRD with the aid of Scherrer's equation[107] or small angle X-ray or neutron scattering can be used if the structures are less than 100 nm.

The interrelations between these quantities listed in Table 3 can be used to check the consistency of measurements or to determine a quantity which is not measured. In the right column, interface density (A_v, area per unit volume) is listed using average feature size (and volume fraction). The number of intersections per length on a random line in a three dimensional space N_l is related to A_v as $N_l = \frac{1}{2} A_v$.[106] Therefore, if the mean intersection length ζ is defined as $\zeta \equiv N_l^{-1} = 2A_v^{-1}$, ζ readily describes the average distance with which phonons encounter boundaries.

6. Beyond κ_l, Tuning Carrier Concentration

Upon quantitatively establishing a successfully structured material, it is necessary to verify the extent to which the optimal carrier concentration can be approached. If the resulting microstructure acts to inhibit electron transport, the resulting nanostructured material would run the risk of removing the benefits from the thermal conductivity reduction. This would lead to a resulting material with an overall lower zT than one started with, an obvious mishap sometimes seen in functional material design.

The most successful system with regard to optimized thermoelectric properties structured via nucleation and growth is the PbTe–Ag_2Te system. Seen in **Figure 19** is the thermal conductivity data for both Na and La doped PbTe. This is a remarkable feat, as the Ag addition not only was a suitable candidate for microstructure generation, but also left the carrier concentration low enough (≈10^{17} cm^{-3}) that it could be considered an intrinsic semiconductor.[29,30] Upon addition of La there was a significant increase in carrier concentration and on account of the Seebeck coefficient optimization, resulted in enhanced thermoelectric properties as an n-type semiconductor. A similar story resulted in the Na doped case, however the conductivity was p-type.

An often encountered problem with carrier concentration control, however, is the generation or depletion of carriers due to the microstructure formation. For example, in the case of Sb_2Te_3 structures in PbTe via nucleation and growth, the equilibrium composition of the cases that have the best results for thermoelectric applications tend to be over doped (n-type) due to excess Sb dissolved in the matrix, well beyond the optimal carrier concentration for n-PbTe.[31] In order to combat this, it would be necessary to counter dope the material with an acceptor impurity (such as an alkali metal) or decrease the amount of residual dopant in the matrix in order to decrease the carrier concentration to the desired level.

Increasing the number of constituent elements in these materials has drawbacks, however. Most high efficiency thermoelectric materials are binary compounds and incorporating an element to generate microstructure transforms them into ternary compounds. The chance of the nanostructured compound having the optimal carrier concentration for thermoelectric purposes is possible but low, so it is expected that a material structured and then extrinsically doped will ultimately be quaternary in nature.

The resulting chemical complexity can lead to solubility limits in these types of materials. For instance, the solubility of Na in PbTe is limited by the inclusion of Ag_2Te as evidenced by the maximum carrier concentration achieved being less than the optimal value in Na doped PbTe without structures.[29,108] While in the case of the extremely low solubility system of Bi and As, the alloying of Bi with Sb increases the solubility of As with respect to (Bi,As) in order to achieve fine microstructure.[109,110] It is unclear whether these limits correspond to a change in thermodynamics, or if the source of the inhibition is the interfacial strain induced by the microstructure. Whatever the case may be, it is important to understand the difficulties associated with microstructure formation of this nature.

The chemical complexity becomes especially important in materials due to either crystal or microstructural anisotropy where directionally dependent transport measurements are necessary to understand the fundamentals governing materials design. Such systems require advanced synthesis techniques for single crystal growth or grain orientation/texturing such as directional solidification or zone melting. However, through rigorous understanding of the phase diagram of a given system it is possible to alleviate this concern because the most important parameters to utilize these synthesis techniques require a critical knowledge of the liquidus and solidus lines. Furthermore, as previously discussed, the nature of the solvus line is vital in certain aspects of microstructure formation and control.

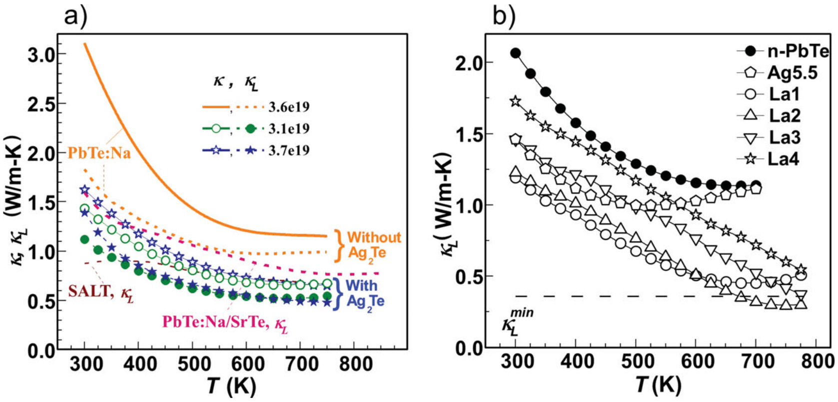

Figure 19. Thermal conductivity data comparing the benefits of the nanostructuring in PbTe composites of Ag_2Te for a) Na[29] and b) La[30] additions. Adapted and reproduced with permission.[29,30] Copyright 2011, The Royal Society of Chemistry; 2011, Wiley-VCH.

© 2013 WILEY-VCH Verlag GmbH & Co. KGaA, Weinheim

7. Conclusions

Presented here are several techniques that involve composite formation and quantitative microstructure control to reduce the lattice thermal conductivity as a means to improve zT for thermoelectric applications. Relevant to microstructure control are the tunable parameters, such as temperature, composition and time, which are the most important first order controls. Here we go beyond these parameters and show how materials design can be controlled when considering other synthesis specific properties such as entropy of fusion, crystal structure similarity, and lattice parameter mismatch. Because much of this microstructure control stems from the energetics and relationships of phases in equilibrium phase diagrams, computational techniques to determine these phase diagrams[111–113] will rapidly become a powerful tool as they become faster and more accurate.

Even though thermal conductivity reduction is a proven method to significantly enhance zT in thermoelectric materials, it will be necessary to move beyond this technique to advance the state of the art. Next generation materials design will have to also incorporate improved electronic properties to see real success as functional materials. However, these advances may be closer to reality than at first glance, as strides are being made in a new avenue of thermoelectric design through band structure engineering techniques.[114] These techniques act to improve the thermoelectric properties by manipulation of the band structure in a material, with examples as simple as alloying to widen band gap [115] or the more intricate band alignment to increase the band degeneracy for a given carrier concentration.[108,116–118]

While the application of band structure modifications is relatively new, it is certainly possible to combine the effects of band structure engineering with thermal conductivity reduction by nanostructuring and achieve a synergistic result. In fact, in the case of the Na doped PbTe–Ag_2Te system it is already taking advantage of the increased band degeneracy of PbTe with sufficient Na doping. The results are not as prominent as one would desire with respect to peak zT because of the limited Na solubility in the presence of Ag_2Te, however the average zT in this material is one of the highest on record due to the near room temperature thermal conductivity reduction.[29]

This is just one of the possibilities regarding the coupling of power factor enhancement and thermal conductivity reduction. While this avenue of thermoelectric optimization has not been fully explored, it is a clear indication that future materials design in bulk thermoelectrics will need to seek simultaneous enhancements of material properties.

Acknowledgements

The authors would like to acknowledge the funding from AFOSR MURI FA9550-10-1-0533 for cryogenic Peltier cooling, support from ARO-MURI W911NF-07-1-0410, Doug Medlin for his tutelage in collecting the transmission electron micrographs and Dominique Schryver's group for their work to create the 3D FIB-SEM image in the article.

Received: August 18, 2013
Revised: October 2, 2013
Published online: December 9, 2013

[1] C. B. Vining, *Nat. Mater.* **2009**, *8*, 83–5.
[2] L. E. Bell, *Science* **2008**, *321*, 1457–61.
[3] A. F. Ioffe, *Semiconductor thermoelements and thermoelectric cooling*, Infosearch **1957**.
[4] W. De Haas, T. Biermasz, *Physica* **1938**, *5*, 320–324.
[5] H. Casimir, *Physica* **1938**, *5*, 495–500.
[6] M. C. Steele, F. D. Rosi, *J. Appl. Phys.* **1958**, *29*, 1517.
[7] D. M. Rowe, V. S. Shukla, N. Savvides, *Nature* **1981**, *290*, 765–766.
[8] Y. Lan, A. J. Minnich, G. Chen, Z. Ren, *Adv. Funct. Mater.* **2010**, *20*, 357–376.
[9] S. K. Bux, J. P. Fleurial, R. B. Kaner, *Chem. Commun.* **2010**, *46*, 8311–24.
[10] H. Wang, A. D. LaLonde, Y. Pei, G. J. Snyder, *Adv. Funct. Mater.* **2012**, *23*, 1586-1596.
[11] M. G. Kanatzidis, *Chem. Mater.* **2010**, *22*, 648–659.
[12] C. J. Vineis, A. Shakouri, A. Majumdar, M. G. Kanatzidis, *Adv. Mater.* **2010**, *22*, 3970–80.
[13] K. Nielsch, J. Bachmann, J. Kimling, H. Böttner, *Adv. Energy Mater.* **2011**, *1*, 713–731.
[14] A. J. Minnich, M. S. Dresselhaus, Z. F. Ren, G. Chen, *Energy Environ. Sci.* **2009**, *2*, 466–479.
[15] M. Zebarjadi, K. Esfarjani, M. S. Dresselhaus, Z. F. Ren, G. Chen, *Energy Environ. Sci.* **2012**, *5*, 5147–5162.
[16] D. L. Medlin, G. J. Snyder, *Curr. Opin. Colloid Interface Sci.* **2009**, *14*, 226–235.
[17] D. L. Medlin, G. J. Snyder, *JOM* **2013**, *65*, 390–400.
[18] G. Schierning, R. Theissmann, N. Stein, N. Petermann, A. Becker, M. Engenhorst, V. Kessler, M. Geller, A. Beckel, H. Wiggers, R. Schmechel, *J. Appl. Phys.* **2011**, *110*, 113515.
[19] B. Zhang, J. He, X. Ji, T. M. Tritt, A. Kumbhar, *Appl. Phys. Lett.* **2006**, *89*, 163114.
[20] P. N. Alboni, X. Ji, J. He, N. Gothard, T. M. Tritt, *J. Appl. Phys.* **2008**, *103*, 113707.
[21] X. Ji, J. He, Z. Su, N. Gothard, T. M. Tritt, *J. Appl. Phys.* **2008**, *104*, 034907.
[22] W. G. Zeier, A. LaLonde, Z. M. Gibbs, C. P. Heinrich, M. Panthöfer, G. J. Snyder, W. Tremel, *J. Am. Chem. Soc.* **2012**, *134*, 7147–54.
[23] J. Embury, R. Fisher, *Acta Metall.* **1966**, *14*, 147–159.
[24] T. Ikeda, L. A. Collins, V. A. Ravi, F. S. Gascoin, S. M. Haile, G. J. Snyder, *Chem. Mater.* **2007**, *19*, 763–767.
[25] T. Ikeda, S. M. Haile, V. A. Ravi, H. Azizgolshani, F. Gascoin, G. J. Snyder, *Acta Mater.* **2007**, *55*, 1227–1239.
[26] T. Ikeda, V. A. Ravi, L. A. Collins, S. M. Haile, G. J. Snyder, *J. Electron. Mater.* **2007**, *36*, 716–720.
[27] T. Ikeda, V. A. Ravi, G. J. Snyder, *Metall. Mater. Trans. A* **2010**, *41A*, 641–650.
[28] G. Edwards, K. Stiller, G. Dunlop, M. Couper, *Acta Mater.* **1998**, *46*, 3893–3904.
[29] Y. Pei, N. A. Heinz, A. LaLonde, G. J. Snyder, *Energy Environ. Sci.* **2011**, *4*, 3640–3645.
[30] Y. Pei, J. Lensch-Falk, E. S. Toberer, D. L. Medlin, G. J. Snyder, *Adv. Funct. Mater.* **2011**, *21*, 241–249.
[31] T. Ikeda, V. A. Ravi, G. J. Snyder, *Acta Mater.* **2009**, *57*, 666–672.
[32] T. Ikeda, N. J. Marolf, K. Bergum, M. B. Toussaint, N. A. Heinz, V. A. Ravi, G. J. Snyder, *Acta Mater.* **2011**, *59*, 2679–2692.
[33] T. Ikeda, M. B. Toussaint, K. Bergum, S. Iwanaga, G. J. Snyder, *J. Mater. Sci.* **2011**, *46*, 3846–3854.
[34] J. D. Hunt, K. Jackson, *Trans. Metall. Soc. AIME* **1966**, *236*, 843–852.
[35] K. Jackson, in *Liquid metals and solidification*, American Society for Metals, Cleveland, Ohio 1958, pp 174–186.
[36] K. Jackson, *Interface structure, in Growth and perfection of crystals*, (eds R. B. Doremus, D. Roberts, Turnbull), John Wiley & Sons, New York 1958, pp 319–324.

© 2013 WILEY-VCH Verlag GmbH & Co. KGaA, Weinheim

[37] D. A. Pawlak, S. Turczynski, M. Gajc, K. Kolodziejak, R. Diduszko, K. Rozniatowski, J. Smalc, I. Vendik, *Adv. Funct. Mater.* **2010**, *20*, 1116–1124.
[38] *CRC handbook of chemistry and physics*, (Ed: D. R. Lide) CRC Press, Boca Raton, FL **2007**.
[39] B. Howlett, S. Misra, M. Bever, *Trans. Metall. Soc. AIME* **1964**, *230*, 1367–1372.
[40] S. Shamsuddin, *Mater. Res. Bull.* **1977**, *12*, 7–12.
[41] O. Kubaschewski, C. Alcock, P. Spencer, *Materials Thermo-Chemistry* 6th ed., Pergamon Press, Tarrytown, NY, 1993.
[42] C. Bale, E. Bélisle, P. Chartrand, S. Decterov, G. Eriksson, K. Hack, I. H. Jung, Y. B. Kang, J. Melançon, A. Pelton, C. Robelin, S. Petersen, *CALPHAD: Comput. Coupling Phase Diagrams Thermochem.* **2009**, *33*, 295–311.
[43] K. J. Lee, C. H. Lee, G. W. Lee, W. S. Hwang, C. H. Lee, S. Yoda, W. S. Cho, *Thermochim. Acta* **2012**, *542*, 37–41.
[44] B. Wei, D. Herlach, B. Feuerbacher, F. Sommer, *Acta Metall. Mater.* **1993**, *41*, 1801–1809.
[45] L. Liu, J. F. Li, Y. H. Zhou, *Acta Mater.* **2011**, *59*, 5558–5567.
[46] W. Tiller, K. Jackson, J. Rutter, B. Chalmers, *Acta Metall.* **1953**, *1*, 428–437.
[47] K. Kuniyoshi, K. Ozono, M. Ikeda, T. Suzuki, S. Kim, W. Kim, *Sci. Technol. Adv. Mater.* **2006**, *7*, 595–600.
[48] B. Chalmers, *Principles of solidification*, John Wiley & Sons, 1964.
[49] H. J. Wu, S. W. Chen, T. Ikeda, G. Snyder, *Acta Mater.* **2012**, *60*, 1129–1138.
[50] H. J. Wu, W. j. Foo, S. w. Chen, G. J. Snyder, *Appl. Phys. Lett.* **2012**, *101*, 023107.
[51] J. W. Cahn, *J. Chem. Phys.* **1965**, *42*, 93.
[52] G. Chadwick, *Prog. Mater. Sci.* **1963**, *12*, 99–182.
[53] S. Gorsse Bauer, P. Pereira, R. Decourt, E. Sellier, *Chem. Mater.* **2010**, *22*, 988–993.
[54] D. Cheetham, N. Ridley, *Metall. Trans.* **1973**, *4*, 2549–2556.
[55] J. Livingston, *J. Cryst. Growth* **1974**, *24*, 94–101.
[56] J. Livingston, J. Cahn, *Acta Metall.* **1974**, *22*, 495–503.
[57] F. Carpay, *Acta Metall.* **1970**, *18*, 747–752.
[58] F. R. N. Nabarro, *Proc. Phys. Soc.* **1940**, *52*, 90–93.
[59] R. D. Doherty, *Physical Metallurgy*, Vol II, New York, North-Holland **1996**.
[60] X. Chen, S. Cao, T. Ikeda, V. Srivastava, G. J. Snyder, D. Schryvers, R. D. James, *Acta Mater.* **2011**, *59*, 6124–6132.
[61] Y. Y. Feutelais, G. Morgant, J. R. Didry, *CALPHAD: Comput. Coupling Phase Diagrams Thermochem.* **1992**, *16*, 111–119.
[62] H. Okamoto, *Binary alloy phase diagrams*, Vol. 1, 2nd ed., ASM International, Materials Park, OH **1990**.
[63] N. A. Heinz, T. Ikeda, G. J. Snyder, D. L. Medlin, *Acta Mater.* **2011**, *59*, 7724–7735.
[64] D. Medlin, J. Sugar, *Script. Mater.* **2010**, *62*, 379–382.
[65] J. L. Lensch-Falk, J. D. Sugar, M. A. Hekmaty, D. L. Medlin, *J. Alloys Compd.* **2010**, *504*, 37–44.
[66] N. Savvides, H. J. Goldsmid, *J. Phys. C: Solid State Phys.* **1980**, *13*, 4671–4678.
[67] N. Savvides, H. J. Goldsmid, *J. Phys. C: Solid State Phys.* **1980**, *13*, 4657–4670.
[68] C. Dames, G. Chen, *Thermoelectrics Handbook: Macro to Nano*, Taylor & Francis.Boca Raton, FL **2006**.
[69] C. B. Vining, W. Laskow, J. O. Van der Hanson, R. R. Beck, P. D. Gorsuch, *J. Appl. Phys.* **1991**, *69*, 4333.
[70] H. Jones, *Mater. Sci. Eng.* **1984**, *65*, 145–156.
[71] D. Bouchard, J. S. Kirkaldy, *Metall. Trans. B* **1997**, *28*, 651–663.
[72] C. Zener, *Trans. Am. Inst. Min., Metall. Pet. Eng.* **1946**, *167*, 550–595.
[73] H. Jones, *Rep. Prog. Phys.* **1973**, *36*, 1425–1497.
[74] H. Liebermann, *Mater. Sci. Eng.* **1980**, *43*, 203–210.
[75] A. L. Greer, *Science* **1995**, *267*, 1947–53.
[76] W. Xie, X. Tang, Y. Yan, Q. Zhang, T. M. Tritt, *Appl. Phys. Lett.* **2009**, *94*, 102111.
[77] H. Li, X. Tang, X. Su, Q. Zhang, C. Uher, *J. Phys. D: Appl. Phys.* **2009**, *42*, 145409.
[78] C. Yu, T. J. Zhu, K. Xiao, J. J. Shen, S. H. Yang, X. B. Zhao, *J. Electron. Mater.* **2009**, *39*, 2008–2012.
[79] S. Y. Wang, W. J. Xie, H. Li, X. F. Tang, Q. J. Zhang, *J. Electron. Mater.* **2011**, *40*, 1150–1157.
[80] A. Jacquot, T. Jürgen, J. Schumann, M. Jägle, H. Böttner, T. Gemming, J. Schmidt, D. Ebling, *J. Mater. Res.* **2011**, *26*, 1773–1784.
[81] L. D. Graham, R. Kraft, *Trans. Metall. Soc. AIME* **1966**, *236*, 94–102.
[82] H. Cline, *Acta Metall.* **1971**, *19*, 481–490.
[83] A. Kolmogorov, *Izv. Akad. Nauk SSSR Ser. Mat.* **1937**, *1*, 355–359.
[84] W. A. Johnson, R. Mehl, *Trans. Am. Inst. Min., Metall. Pet. Eng.* **1939**, *135*, 416–442.
[85] M. Avrami, *J. Chem. Phys.* **1939**, *7*, 1103.
[86] M. Avrami, *J. Chem. Phys.* **1940**, *8*, 212.
[87] M. Avrami, *J. Chem. Phys.* **1941**, *9*, 177.
[88] F. Yang, T. Ikeda, G. J. Snyder, C. Dames, *J. Appl. Phys.* **2010**, *108*.
[89] T. Ikeda, V. A. Ravi, G. J. Snyder, *J. Mater. Res.* **2011**, *23*, 2538–2544.
[90] H. Hardy, T. Heal, *Prog. Met. Phys.* **1954**, *5*, 143–278.
[91] J. Burns, *Trans. Am. Inst. Min., Metall. Pet. Eng.* **1934**, *113*, 239–261.
[92] P. Merica, R. Waltenberg, H. Scott, *Trans. Am. Inst. Min., Metall. Pet. Eng.* **1921**, *64*, 41–77.
[93] K. Bergum, T. Ikeda, G. J. Snyder, *J. Solid State Chem.* **2011**, *184*, 2543–2552.
[94] N. A. Heinz, T. Ikeda, G. J. Snyder, *Acta Mater.* **2012**, *60*, 4461–4467.
[95] D. A. Porter, K. E. Easterling, *Phase Transformations in Metals and Alloys*, 2nd ed. CRC Press, **2001**.
[96] M. S. Jeng, R. Yang, D. Song, G. Chen, *J. Heat Transfer* **2008**, *130*, 42410.
[97] K. C. Russell, *Adv. Colloid Interface Sci.* **1980**, *13*, 205–318.
[98] D. Turnbull, *Metall. Mater. Trans. A* **1981**, *12*, 695–708.
[99] Y. F. Ouyang, X. P. Zhong, W. M. Wu, *Sci. China, Ser. A: Math., Phys., Astron.* **2000**, *43*, 180–184.
[100] J. Eckert, L. Schultz, K. Urban, *J. Non-Cryst. Solids* **1991**, *127*, 90–96.
[101] J. Xu, J. H. He, E. Ma, *Metall. Mater. Trans. A* **1997**, *28*, 1569–1580.
[102] T. Ikeda, L. Haviez, Y. Li, G. J. Snyder, *Small* **2012**, *8*, 2350–5.
[103] J. W. Cahn, R. Fullman, *Trans. Am. Inst. Min., Metall. Pet. Eng.* **1956**, *206*, 610–612.
[104] J. He, S. N. Girard, M. G. Kanatzidis, V. P. Dravid, *Adv. Funct. Mat.* **2010**, *20*, 764–772.
[105] J. Callaway H. von Baeyer, *Phys. Rev.* **1960**, *120*, 1149–1154.
[106] J. C. Russ, *Practical Stereology*, Plenum Press **1986**.
[107] B. Cullity, S. Stock, *Elements of x-ray diffraction* 3rd ed., Prentice Hall, **2001**.
[108] Y. Pei, X. Shi, A. LaLonde, H. Wang, L. Chen, G. J. Snyder, *Nature* **2011**, *473*, 66–9.
[109] G. V. Semenova, T. P. Sushkova, V. S. Gorshkov, *Russ. J. Inorg. Chem.* **2006**, *51*, 1504–1508.
[110] N. A. Heinz, S. Howell, H. Wang, T. Ikeda, G. J. Snyder, *Phys. Status Solidi A* **2012**, *209*, 2565–2569.
[111] S. Barabash, V. Ozolins, C. Wolverton, *Phys. Rev. Lett.* **2008**, *101*.
[112] S. Barabash, V. Ozolins, C. Wolverton, *Phys. Rev. B.* **2008**, *78*.
[113] G. Pomrehn, E. Toberer, G. Snyder, A. van de Walle, *Phys. Rev. B.* **2011**, *83*.
[114] Y. Pei, H. Wang, G. J. Snyder, *Adv. Mater.* **2012**, *24*, 6125--6135.
[115] Y. Pei, N. A. Heinz, G. J. Snyder, *J. Mater. Chem.* **2011**, *21*, 18 256.
[116] Y. Pei, H. Wang, Z. M. Gibbs, A. D. LaLonde, G. J. Snyder, *NPG Asia Mater.* **2012**, *4*, e28.
[117] Y. Pei, A. D. LaLonde, N. A. Heinz, G. J. Snyder, *Adv. Energy Mater.* **2012**, *2*, 670–675.
[118] Y. Pei, A. D. LaLonde, N. A. Heinz, X. Shi, S. Iwanaga, H. Wang, L. Chen, G. J. Snyder, *Adv. Mater.* **2011**, *23*, 5674–8.

© 2013 WILEY-VCH Verlag GmbH & Co. KGaA, Weinheim